Volume 1, Number 1 *December 2019*

Nanomaterials Science & Engineering

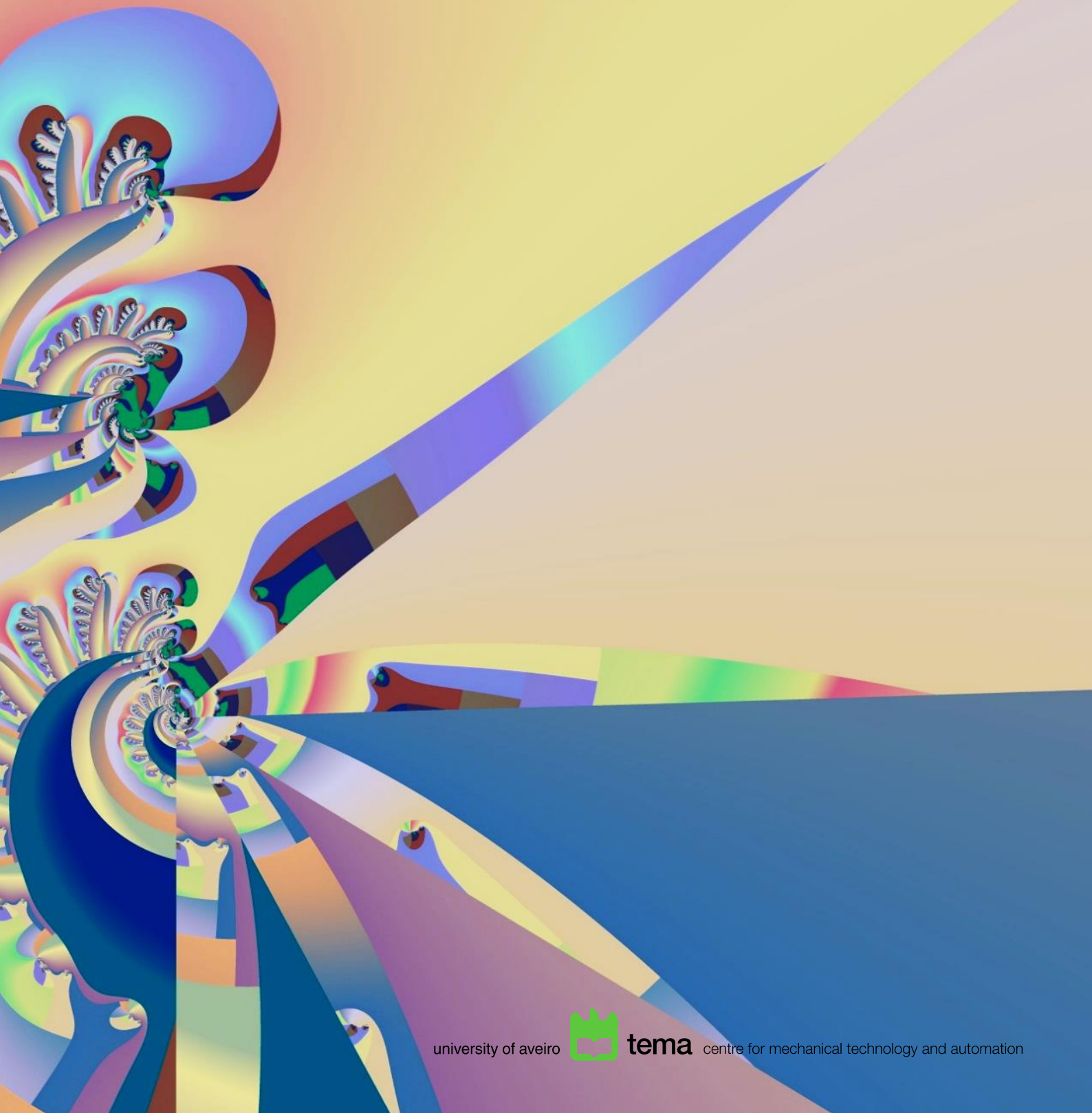

university of aveiro tema centre for mechanical technology and automation

Volume 1, Number 1 *December 2019*

Nanomaterials Science & Engineering

university of aveiro tema centre for mechanical technology and automation

Title
Nanomaterials Science & Engineering (NMS&E), Vol.1, No.1, 2019

Publisher
University of Aveiro

Support
Serviços de Biblioteca, Informação Documental e Museologia
Centre for Mechanical Technology & Automation (TEMA)
Mechanical Engineering Department
University of Aveiro

Mailing Address
Department of Mechanical Engineering
University of Aveiro
Aveiro 3810-193
Portugal
E-mail: bdikin@ua.pt

ISSN: 2184-7002

December 2019
University of Aveiro

Welcome to the first issue of the Journal of Nanomaterials Science & Engineering (NMS&E). NMS&E is a peer-reviewed journal communicating scientific and technological advances in the fields of the new materials and technology at the nanoscale. The journal provides scientists and the technology business community with the latest developments in Nanomaterials Science.

Editors-in-Chief

Igor Bdikin
Paula Alexandrina de Aguiar Pereira Marques
Duncan Paul Fagg

NANOMATERIALS SCIENCE & ENGINEERING
Vol. 1, No. 1, pp. 6-9 (2019)

RESEARCH ARTICLE

https://proa.ua.pt/index.php/nmse/

XPS study of the thermal vapour sulfurization of tungsten thin films

María J. Hortigüela* and Gonzalo Otero-Irurueta*

Centre for Mechanical Technology & Automation (TEMA), University of Aveiro, 3810-193 Aveiro, Portugal
**Corresponding authors, e-mail address: mhortiguela@ua.pt (M.J. Hortigüela) and otero.gonzalo@ua.pt (G. Otero-Irurueta)*

Received 22 October 2019; accepted 29 November 2019; published online 19 December 2019

ABSTRACT

Here we report the XPS spectra of thermally sulfurized tungsten thin films on SiO_2 at different temperatures. The sulfurization was performed in a chemical vapour deposition system at 400 ºC, 500 ºC, 550 ºC, 600 ºC and 750 ºC. Below 500 ºC XPS showed that the tungsten layer was oxidized (W^{6+}) and only carbon-sulfur compounds were detected. On the other hand, from 600 ºC the sulfurization process was complete by forming WS_2, while at the intermediate temperature of 550 ºC the films were partially oxidized and partially sulfurized.

1. INTRODUCTION

Transition metal dichalcogenides (TMDs) are quite promising 2D materials due to their amazing properties [1-4]. They follow the general form of MX_2 in which M and X are transition metal and chalcogen atoms, respectively. Among others transition metals, molybdenum and tungsten are the most used, producing MoS_2 and WS_2 when sulfurized, respectively. Nowadays, these materials are subject of intense research around the world due to the broad range of their possible applications [5]. Thus, several applications in fields such as nanoelectronics [1], optoelectronics [6], spintronics [6] and energy conversion [7,8], among others, have been proposed. Nevertheless, the development of low-cost techniques for synthesising thin films of TMDs for the above-mentioned applications remains an ongoing challenge.

The most used methods for the synthesis of TMDs are liquid exfoliation [9] and chemical vapour deposition (CVD) [9,10], which usually produce inhomogeneous samples. On the other hand, thermal vapour sulfurization (TVS) [11,12] seems to be better positioned for growing large-area high-quality TMDs. It consists in a two-step process in which a transition metal is firstly deposited on a substrate and then sulfurized in a CVD system [11,13,14]. Nowadays, there is a huge research on both the method for pre-depositing the metal on a substrate as well as the conditions for its sulfurization [11]. In fact, metal deposition have been carried out by following different chemical and physical methods, such as drop coating, atomic layer deposition, sputtering, pulsed laser deposition and thermal evaporation [14].

In this work, we characterized by X-ray photoelectron spectroscopy (XPS) the TVS of tungsten layers at different temperatures to obtain WS_2. Tungsten was deposited on SiO_2 by thermal evaporation from a filament under vacuum conditions. This report shows that W remains oxidized when the TVS is carried out at temperatures lower than 500 ºC. On the other hand, for temperatures higher than 600 ºC the TVS process is complete, forming WS_2 on SiO_2.

2. METHODS

SiO_2 substrates were cleaned with acetone and ethanol in an ultra-sonic system.

A tungsten wire with a diameter of 0.25 mm was used for W thermal deposition on SiO_2 at an

electrical current of 10 A under a pressure of $5x10^{-3}$ mbar.

The sulfurization was carried out in a CVD system, where sulfur powder was heated at 170 ºC while the sample temperature was ramped at 10 ºC/min until reaching the target value. A combination of N_2 (4 l/h) and H_2 (1 l/h) was used during TVS at a pressure of 10 mbar.

XPS spectra were acquired in an Ultra High Vacuum (UHV) system with a base pressure of $2x10^{-10}$ mbar. The system is equipped with a hemispherical electron energy analyzer (SPECS Phoibos 150), a delay-line detector and a monochromatic AlKα (1486.74 eV) X-ray source. High-resolution spectra were recorded at normal emission take-off angle and with a pass-energy of 20 eV, which provides an overall instrumental peak broadening of 0.5 eV.

3. RESULTS

First, a desired quantity of tungsten was deposited on SiO_2 by thermal evaporation under vacuum conditions. This evaporation was performed by flowing an electric current through a tungsten filament. Then, the samples were introduced in a CVD system for their sulfurization following an optimized procedure described in [11]. Roughly, the samples were introduced at the heating zone of a CVD system while an alumina boat containing S was located at the entrance of the quartz tube and independently heated.

Figure 1 shows a scheme of a tungsten thin film growth and its subsequent thermal vapour sulfurization.

The TVS of tungsten layers was followed by XPS. This technique allows to detect the elements at the sample and their chemical environment. Figure 2 shows the XPS results obtained after TVS at 400 ºC, 500 ºC, 550 ºC, 600 ºC and 750 ºC. Figure 2a, 2b and 2c show the W 4f, S 2p and O 1s XPS regions, respectively. Moreover, W $5p_{3/2}$ appears at higher binding energies (BE) of Figure 2a.

Two different regimes were identified by XPS, below 500 ºC (black and red spectra in Fig. 2) and above 600 ºC (blue and violet spectra in Fig. 2). Moreover, at an intermediate temperature of 550 ºC (green spectra in Fig. 2) the shape of W 4f, S 2p and O 1s XPS spectra can be described as the convolution of the low and high temperature spectra (see below).

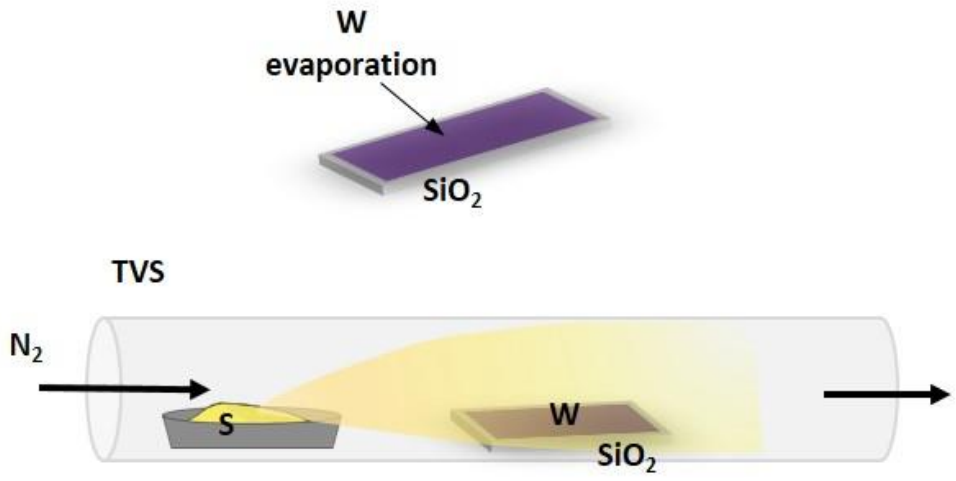

Figure 1. Scheme of the protocol used for growing WS_2 thin films. A pre-deposited W film on SiO_2 was thermally vapour sulfurized.

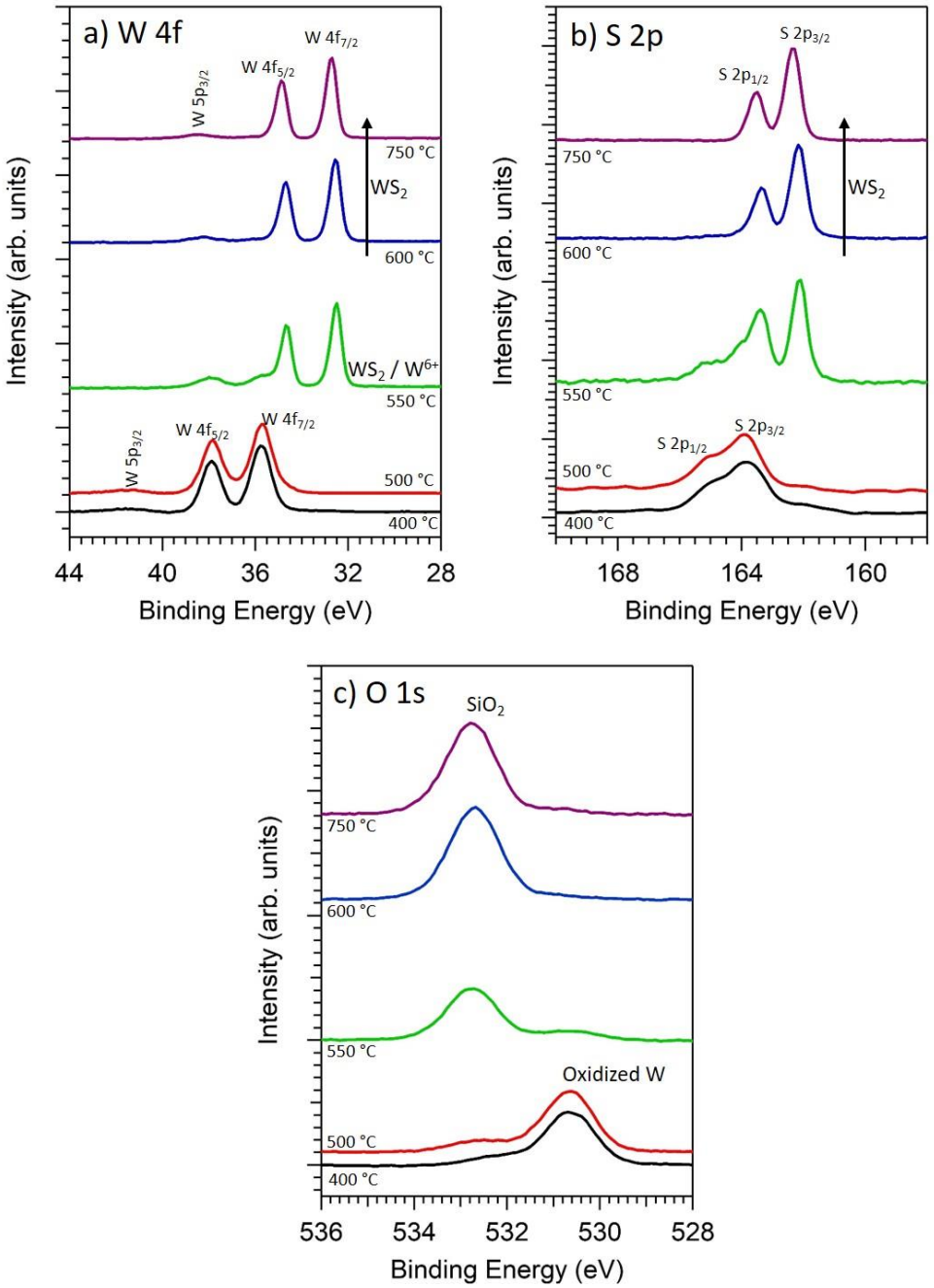

Figure 2. XPS normalized spectra of the tungsten thin film after thermal vapour sulfurization at 400 ºC (black spectra), 500 ºC (red), 550 ºC (green) and 600 ºC (blue) and 750ºC (violet). a) W 4f, b) S 2p and c) O 1s regions.

Below 500 ºC, W 4f had two main XPS peaks centred at BEs of about 35.8 eV and 37.9 eV, ascribed to W $4f_{7/2}$ and W $4f_{5/2}$, respectively. These BEs were in good agreement with previous reported values for oxidized tungsten *i.e.* W^{6+} [15-18]. On the other hand, in the low temperature regime, S 2p showed two broad peaks centred at BEs of about 163.9 eV and 165.1 eV corresponding with S $2p_{3/2}$ and S $2p_{1/2}$, respectively. These BEs are higher than the expected values for S atoms in a WS_2 chemical environment (blue spectra of Fig. 2b). On the contrary, XPS indicated that at the low temperature regime, some sulphur atoms were deposited on oxidized tungsten film but not forming

WS_2. In fact, these BE values are compatible with C-S species, suggesting the presence of some organo-sulfur compounds [19]. Importantly, the S/W ratio obtained by XPS at the low temperature regime was 0.58, significantly lower than that expected for WS_2. Moreover, two peaks appeared in the O 1s region at BEs of about 532.8 eV and 530.7 eV. The peak at higher BE was ascribed to the oxygen atoms of the SiO_2 [20] substrate while the second peak corresponded with WO_3 [17,18].

A completely different scenario was obtained by XPS at temperatures higher than 600 ºC in which both W 4f and S 2p strongly shifted to lower BEs. W 4f had two main peaks centred at BEs of about 32.6 eV (W $4f_{7/2}$) and 34.7 eV (W $4f_{5/2}$), values which were in good agreement with previous reported BEs for W atoms in a WS_2 chemical environment [15,16,21]. Moreover, the extra peak centred at a BE of 38.3 eV was ascribed to W $5p_{3/2}$ from WS_2 samples [15,16,22]. Complementary, S 2p presented two sharp peaks at BEs of 162.2 eV (S $2p_{3/2}$) and 163.4 eV (S $2p_{1/2}$) as it was expected for sulfur atoms in WS_2 samples [15,16,21,22]. Thus, XPS indicated that WO_3 transformed into WS_2 after TVS at temperatures higher than 600 ºC. Accordingly, the peak ascribed to WO_3 in the O 1s XPS region vanished in the high temperature regime (see Fig. 2c).

4. CONCLUSIONS

XPS analysis of the thermal vapour sulfurization of oxidized tungsten thin films on SiO_2 showed that the reaction started at temperatures higher than 500 ºC, although the complete transformation to WS_2 was obtained from 600 ºC. Thus, at the intermediate temperature of 550 ºC, the films were partially oxidized and partially sulfurized. In XPS spectra of WS_2 films obtained from 600 ºC W $4f_{7/2}$ was centred at a BE of around 32.6 eV while S $2p_{3/2}$ appeared at 162.2 eV.

ACKNOWLEDGMENTS

We acknowledge the financial support from Fundação para a Ciência e Tecnologia (FCT), Portugal. G O-I and M J H thank FCT for their respective contracts (IF/01054/2015 and BI/UI66/6867/2017). TEMA researchers thank TEMA for its financial support (UID/EMS/00481/2019).

REFERENCES

[1] S. Manzeli, D. Ovchinnikov, D. Pasquier, O. V. Yazyev and A. Kis, *Nat. Rev. Mater.* **2**, 17033 (2017).
[2] G.H. Han, D.L. Duong, D.H. Keum, S.J. Yun and Y.H. Lee, *Chem. Rev.* **118**, 6297 (2018).
[3] W. Choi, N. Choudhary, G.H. Han, J. Park, D. Akinwande and Y.H. Lee, *Mater. Today.* **20**, 116 (2017).
[4] X. Duan, C. Wang, A. Pan, R. Yu and X. Duan, *Chem. Soc. Rev.* **44**, 8859 (2015).
[5] S.A. Han, R. Bhatia and S-W. Kim, *Nano Converg.* **2**, 17 (2015).
[6] V. Sorkin, H. Pan, H. Shi, S. Y. Quek and Y.W. Zhang, *Crit. Rev. Solid State Mater. Sci.* **39**, 319 (2014).
[7] H. Li, X. Jia, Q. Zhang and X. Wang, *Chem.* **4**, 1510 (2018).
[8] X. Yu and K. Sivula, *ACS Energy Lett.* **1**, 315(2016).
[9] H. Wang, C. Li, P. Fang, Z. Zhang and J. Z. Zhang, *Chem. Soc. Rev.* **47**, 6101 (2018).
[10] D. K. Sharma, E. V. Ramana, S. Fateixa, M. J. Hortigüela, G. Otero-Irurueta, H. I. S. Nogueira and A. Kholkin, *Mater. Res. Bull.* **97**, 265 (2018).
[11] M. J. Hortigüela, I. Bdikin and G. Otero-Irurueta, *Thin Solid Films* **691**, 137588 (2019).
[12] I. Hotovy, L. Spiess, M. Sojkova, I. Kostic, M. Mikolasek, M. Predanocy, H. Romanus, M. Hulman and V. Rehacek, *Appl. Surf. Sci.* **461**, 133 (2018).
[13] C-R. Wu, X-R. Chang, C-H. Wu and S-Y. Lin, *Sci. Rep.* **7**, 42146 (2017).
[14] H. F. Liu, S. L. Wong and D. Z. Chi, *Chem. Vap. Depos.* **21**, 241 (2015).
[15] L. Wu, A. J. F. van Hoof, N. Y. Dzade, L. Gao, M. I. Richard, H. Friedrich, N. H. De Leeuw, E. J. M. Hensen and J. P. Hofmann, *Phys. Chem. Chem. Phys.* **21**, 6071 (2019).
[16] F. Perrozzi, S. M. Emamjomeh, V. Paolucci, G. Taglieri, L. Ottaviano and C. Cantalini, *Sensors Actuators B Chem*. **243**, 812 (2017).
[17] R. Ji, D. Zheng, C. Zhou, J. Cheng, J. Yu and L. Li, *Materials* **10**, 820 (2017).
[18] S. Li, Z. Yao, J. Zhou, R. Zhang and H. Shen, *Mater. Lett.* **195**, 213 (2017).
[19] T. Liu, Z-W. Cui, J. Zhou, Y. Wang, Z-g. Zou, *Nanoscale Res. Lett.* **12**, 375 (2017).
[20] T. V. Larina, L. S. Dovlitova, V. V. Kaichev, V. V. Malakhov, T.S. Glazneva, E. A. Paukshtis and B. S. Bal'zhinimaev, *RSC Adv.* **5**, 79898 (2015).
[21] D. Escalera-López, R. Griffin, M. Isaacs, K. Wilson, R. E. Palmer and N. V. Rees, *Appl. Mater. Today* **11**, 70 (2018).
[22] A. P. Shpak, A. M. Korduban, L. M. Kulikov, T. V. Kryshchuk, N. B. Konig and V. O. Kandyba, *J. Electron Spectros. Relat. Phenomena.* **181**, 234 (2010).

NANOMATERIALS SCIENCE & ENGINEERING
Vol. 1, No. 1, pp. 10-21 (2019)

RESEARCH ARTICLE

https://proa.ua.pt/index.php/nmse/

Piezoelectric, ferroelectric, optoelectronic phenomena in hydroxyapatite by first-principles and with various defects

V. S. Bystrov[1*], Jose Coutinho[2], L. A. Avakyan[3], A.V. Bystrova[1,4], E.V. Paramonova[1]

[1]Institute of Mathematical Problems of Biology, Keldysh Institute of Applied Mathematics, RAS, 142290 Pushchino, Moscow region, Russia
[2]Department of Physics & I3N, University of Aveiro, Campus Santiago, 3810-193 Aveiro, Portugal
[3]Physics Faculty, Southern Federal University, Zorge Street 5, Rostov-on-Don 344090, Russia
[4]Institute of Biomedical Engineering and Nanotechnologies, Riga Technical University, Riga, Latvia
**Corresponding author, e-mail address: vsbys@mail.ru, bystrov@impb.ru*

Received 21 October 2019; accepted 2 December 2019; published online 19 December 2019

ABSTRACT

The results are based on DFT calculations of hydroxyapatite (HAP) structures, pristine and defective, determined by various defects formed by Oxygen vacancy dependent on its charged states. Ordered hexagonal and monoclinic HAP phases have own spontaneous polarization, while disordered do not have it. These ferroelectric properties determined by orientation of OH dipoles provide piezoelectric and pyroelectric phenomena in such HAP structures for which all corresponding values and coefficients were investigated and calculated in this paper. The optical properties of defective HAP are mainly determined by various types of Oxygen vacancy defects (as well as hydroxyl OH group vacancy) and can lead to absorption and photocatalysis under ultraviolet illumination. The hybrid density functional theory (DFT) approaches of the structural and electronic properties of oxygen vacancies in large HAP supercells within the plane-wave formalism were mainly used in this work. The vacancies were investigated in large supercells, for which formation energies and electronic transition energies were calculated. The calculations were carried out using DFT, as implemented by the (Vienna ab initio package) VASP. The exchange-correlation potential was evaluated either using the generalized gradient approximation according to PBE functional or the three-parameter hybrid B3LYP functional, which incorporates a fraction of exact exchange with local and semi-local functional. These methods are also applied to the calculation of defect levels. Several other methods, such as AIMPRO and HyperChem, were used too, for several necessary cases and comparison. As a result, the main new features of pristine and defective HAP were established and analysed from first-principles.

1. INTRODUCTION

Hydroxyapatite (HAP) is an important natural and mineral component of mammal bones and teeth of vertebrates in humans and animals [1], which is used in prosthetic bio-implants [2]. Together with the organic bone's component (collagen) and living bone cells (osteoclasts, osteoblasts and osteocytes) [1−4] HAP crystallizes as an array of stand-alone HAP platelet compositions or needle-like nanocrystals in the gaps of laid tropocollagen fibrils, forming and strengthening the bone structure [4-7]. Due to its natural innate biological activity, HAP is widely used in medicine for manufacturing bone and dental implants (both filler and coating material for titanium and similar implants) [2-5], for bone replacement and regeneration [1-8]. However, despite the importance of HAP in medicine, several promising

new applications of this material (e.g., in photo-catalysis [9]), depend on how well we understand its fundamental properties.

HAP has specific structural features that determine its basic physical properties, charge distribution, and surface electric potential, which play a particularly important role in the adhesion and proliferation of living cells [1-8]. A distinctive feature of HAP is that it has a specific direction of the formation of hydroxyl OH groups (internal OH channels) along the c axis, which allows protons to be transported along this axis under special conditions [5, 8, 10, 11]. Formation of internal polarization along these OH channels creates a directional distribution of surface charge density. This is very important for the adhesion of living cells, their growth and proliferation.

Constantly growing interest of researchers to the studies of hydroxyapatite in the world shows that this material has a unique complete of physical properties. Several years ago it was considered only as a structure of a centrosymmetric crystal, but by now it has been established that it has noncentrosymmetric structural properties [12-17]. Recent studies have shown that HAP exhibits both piezoelectric, pyroelectric and, in whole, ferroelectric properties [8, 12-17]. A number of theoretical studies of the structure and properties of HAP have been carried out [18-21]. They showed the value of the d_{33} piezoelectric coefficient ~ 16 pC/N [20] which is in good agreement with the experimental study as described in [15, 17]. And, in addition, it turns out that HAP has important photocatalytic properties [22-24]. This is due to the electronic features of existing defects in HAP, especially due to oxygen vacancies [24]. Further, experimental evidence suggests that oxygen vacancies play a critical role in the production of surface radicals upon exposure of HAP to ultraviolet (UV) light. However, very little is known about the underlying physical and chemical details for these processes in the HAP. Moreover, in various fields of application HAP demonstrates different properties. So, for example, it turned out that its polar properties are important for biomedicine and implantology.

In this article, we analyze the polarization values obtained for various HAP models and the calculation methods used [8, 18-21, 24-29] in comparison with various experimental data [11-17, 20, 21, 30, 31]. All relevant ferroelectric effects are also evaluated and analyzed: piezoelectric and pyroelectric coefficients were estimated and compared [21]. Optical properties, in particular photocatalytic properties, which are especially affected by defects such as oxygen vacancies with various charges and structural features, are also taken into account [25, 26].

For all these aims the novel developments of the hybrid density functional theory (DFT) in the structural and electronic properties of oxygen vacancies in large HAP supercells within the plane-wave formalism [25, 26] were mainly used in this work. The vacancies were investigated in large supercells, for which formation energies and electronic transition energies were calculated. The calculations were carried out using DFT, as implemented by the (Vienna ab initio package) VASP [28]. The exchange-correlation potential was evaluated either using the generalized gradient approximation according to PBE functional or the three-parameter hybrid B3LYP functional, which incorporates a fraction of exact exchange with local and semi-local functional [25]. These methods are also applied to the calculation of defect levels [26]. Several other methods, such as AIMPRO [27] and HyperChem [29], were used too, for several necessary cases and comparison. As a result, the main new features of pristine and defective HAP were established and analysed from first-principles.

2. COMPUTATIONAL DETAILS AND MODELS

The calculations of pristine and defective HAP structures and properties were carried out from first principles using DFT by AIMPRO code (in Local Density Approximation (LDA)) [27] and by VASP [28] (in Generalized Gradient Approximation (GGA) according to Perdew, Burke, Ernzerhof (PBE) approach and with Becke three-parameter (B3LYP) hybrid functional [25, 26]) in combination with semi-empirical quantum-chemical (QM) PM3 method from HypemChem 8.0 package [29]. More computational details are described in [25, 26]. The main peculiarity of this study is the introduction of the supercells model made up of 2x2x2 = 8 polar HAP unit cells (space group $P6_3$) for hexagonal HAP phase both for pristine and defective HAP with oxygen vacancies. The monoclinic phase

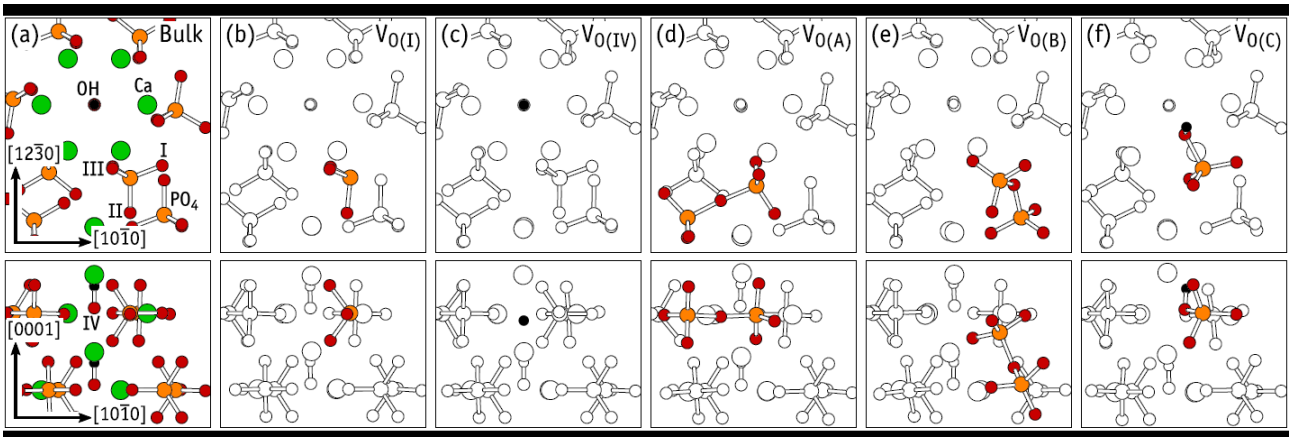

Figure1. Atomistic diagrams showing the structure of a pristine region of HAP (Bulk), along with structures I, IV, A, B and C of V_O defects. Upper and lower insets correspond to the same structures viewed along [0001] and [1230] directions of the hexagonal lattice, respectively. On the bulk diagrams, Ca, P, O and H atoms are shown in green, orange, red and black, respectively. The four different oxygen sites are indicated with I,..., IV labels. On defect diagrams, only atoms neighbouring the defect are coloured. (Adapted and modified with permission from [26]. Copyright (2019) American Chemical Society).

$P2_1/b$ is more stable, but it differs a little only by 25 meV per unit cell [19], with their electronic structures being the same. Crystalline HAP has oxygen atoms on four symmetry inequivalent sites, which are referred to as oxygen types I−IV. Types I, II, and III are in the phosphate units, while type IV oxygen atoms are located in the OH− anions. These are denoted as O(I), ..., O(IV) (oxygen vacancy V_O(I),…, V_O(IV), Fig. 1) and they were analysed in [26]. In all these calculations we take account of full relaxation of the cell, including adjusting the atomic positions and the cell shape (total optimization of the structure). But, a full relaxation of such large HAP supercells (as 2x2x2 = 8 polar HAP unit cells) using plane-wave hybrid-DFT is prohibitively expensive. Instead, defect structures were first found by relaxing all atomic coordinates within PBE (it is step 1 of calculations). The resulting structures were used at the second step (step 2 of calculations), where the total energy was obtained within hybrid-DFT by means of the B3LYP single-point calculation. This procedure was necessary due to the sheer size of the Hamiltonian at hand combined with the use of a plane-wave method. All defect calculations employed a Γ-point sampling [25, 26]. The optimized data obtained for each HAP structure, were taken out and transformed to a format of HyperChem files [29] for calculations of their physical properties, particularly, polarization. For present calculations we use semi-empirical quantum mechanics methods PM3 method in restricted and unrestricted Hartree-Fock approximation (RHF/UHF).

3. MAIN RESULTS AND DISCUSSIONS

Recently computed data show, first, that HAP can co-exist in different phases: hexagonal and monoclinic [8, 19]. Now we are especially interested in an ordered hexagonal structure, which could demonstrate piezoelectric and pyroelectric properties as well [20, 21]. For instance, the energy difference between HAP unit cells with $P6_3$ and $P6_3/m$ symmetry (the latter being obtained by aligning the OH units along opposite directions in their big supercell model) is E($P6_3/m$) − E($P6_3$) = 0.39 eV with both energies being obtained from fully relaxed B3LYP-level calculations [26]. This result is in line with computed difference E($P6_3/m$) − E($P6_3$) = ~ 0.132 eV/unit cell in LDA approximation [19].

3.1. Polarization and following piezo-electric and pyro-electric - ferroelectric effects

To calculate the polarization for different HAP phases we construct simplest models, including mainly the OH-channels with various orientations of the OH dipoles (see on Fig. 2). Table 1 present polarization data obtained by calculations of these

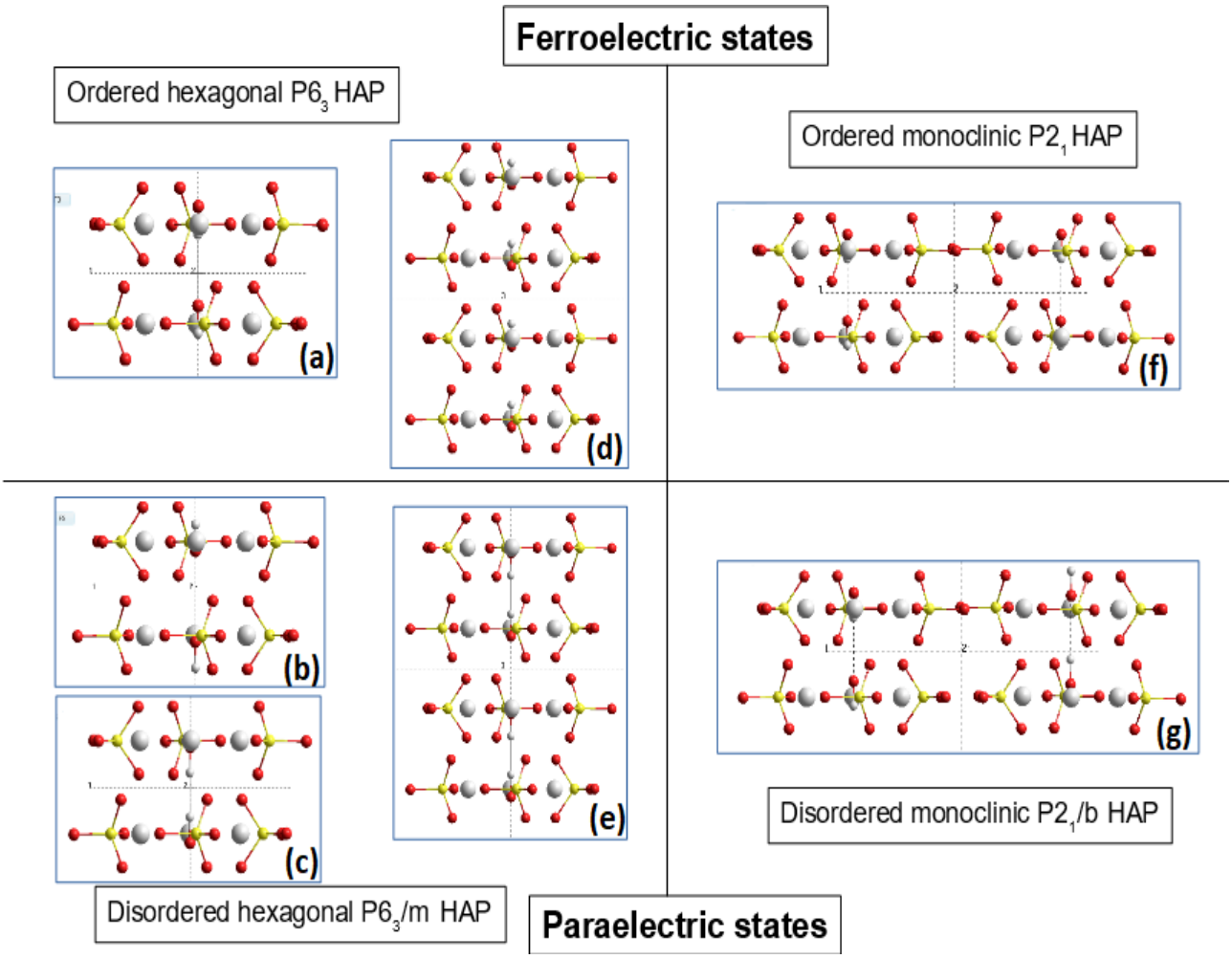

Figure 2. Schematics of OH electric dipole orientation and switching from paraelectric (disordered) to ferroelectric (polar and ordered) states of the hexagonal and monoclinic HAP:

a), d) – 1 and 2 units $P6_3$ polar ordered model with parallel orientation of the OH dipoles;

b), c) and e) – 1 unit models with various ant-parallel 11 and 22 (opposite) OH dipoles orientation, and 2 units - $P6_3/m$ model;

f), g) – monoclinic polar ordered polar $P2_1$ and disordered non-polar $P2_1/b$ models.

models in comparison with other data.

The data obtained by these calculations in comparison with other data computed and measured for HAP polarization values in their different phases clearly show, that namely ordering of the OH dipoles determine the existing of the polar HAP phase (with total sum of polarization directed along the OH-channel and coincides with c-axis) and its switching between paraelectric (disoredered hexagonal $P6_3/m$) and ferroelectric (polar and ordered hexagonal $P6_3$). The polarization values in the ferroelectric phase for different approaches are comparable and are of the order of P ~ 0.02 – 0.12 C/m^2 (Table 1), while in paraelectric (non-polar) phase all different models show values close to zero, due to compensation of an opposite anti-parallel orientation of OH groups along these OH-channels, but it is not equal exactly P = 0. It has some deviation around zero sum of total polarization by a several small values ~ 0.001 C/m^2, that arise due some local fluctuations in the atomic positions and the OH dipole orientations.

Table 1. Polarization in HAP calculated by PM3 method after VASP in comparison with other data

	Model/Method/ Space Group		Hexagonal RHF, C/m^2		Hexagonal UHF, C/m^2		Monoclinic RHF, C/m^2		Other data refs
			Pz	Pt	Pz	Pt	Pz	Pt	
1 unit model	OH-OH par1	$P6_3$	**0.0111**	**0.031**	**-0.030**	**0.107**			
	HO-HO par3	$P6_3$	**-0.011**	**0.029**	**-0.054**	**0.118**			
	OH-HO 22	$P6_3/m$	*-0.004*	*0.005*	*0.002*	*0.002*			
	HO-OH 11	$P6_3/m$	*-0.001*	*0.002*	*0.001*	*0.002*			
2 unit model	OH-OH par 0	$P6_3$ $P2_1$	**0.02** **-**	**0.027** **-**	**-0.075** **-**	**0.127** **-**	**-** **-0.020**	**-** **0.064**	
	OH anti-par 1	$P6_3/m$ $P2_1/b$	*0.0012* -	*0.013* -			- *-0.004*	- *0.006*	
	OH anti-par 2	$P6_3/m$	*-0.001*	*0.011*					
Various method (for ordered HAP)	AIMPRO par	$P2_1$ $P6_3$	- **-0.018**	**-**			**-0.021** **-**	-	Bystrov [20, 21], using HyperChem /AIMPRO
	VASP	$P6_3$ $P2_1$	**-0.0705** **-**				**-** **-0.0987**		Shunbo Hu, et al [31]
	HyperChem		**~ 0.046 – 0.112 (up ~ 0.18)**						Bystrov et al. [18, 35]
	Experimental		**Up to ~ 0.149**						Nakamura et al [11]
	AFM Experim.		**From 0.005 up to ~ 0.072**						Vandiver et al [32]
	Experim. vary		**~ 0.1 – 0.2**						Lang,Tofail et al [12-17]

*) Here “par” denotes ‘parallel” orientation of OH group (dipoles), “anti-par” - “anti-parallel”

Note, that the accuracy of these calculations was determined by the convergence limit at the level of ~ 0.001 (due to HyperChem software option [20, 29] for the PM3 method calculations).

The monoclinic phase $P2_1/b$ (disordered and paraelectric) is a little more stable (than $P6_3/m$), but it differs only on 25 meV per unit cell [21] (as mentioned above). The similar relation as for hexagonal phases is existing between of the ordered polar monoclinic HAP phase with $P2_1$ space group and disordered HAP phase with anti-parallel OH dipoles orientation in $P2_1/b$ space group. All these relations are shown on the schematics presented on Fig. 2 and Table 1.

This effect may be due to restriction of the models, but may reveal some nonsymmetrical HAP structures. In any case, it is well known that a full ideal periodical crystal structure for HAP does not exist in real nature. More or less all HAP structures have many deviations from an ideal crystal: non-stoichiometry, replacements, insertions, vacancies etc. Especially important role belongs to oxygen

vacancies of different types [26]. We consider some results of the influence of such defects below.

But for all ordered HAP structures, as pristine as well defective, the existence of such spontaneous polarization led (as in any ferroelectric) to the pyroelectric and piezoelectric phenomena. Now the values of the piezoelectric coefficients are well known and are determined by calculations and measurements d_{33} ~ 6.4 – 8.5 pm/V (or pC/N) for hexagonal $P6_3$ HAP, and of the order of d_{33} ~ 15.7 – 16.5 pm/V (or pC/N) for monoclinic $P2_1$ HAP [15-17, 20, 21, 30]. For the values of pyroelectric coefficients, the estimation for the HAP in the hexagonal phase yields the value 10–100 $\mu C/(m^2K)$, which is in line with experimental observations (p ~ 12 $\mu C/(m^2 K)$ [14-17].

It is interesting to note, first, that recent calculations of polarization in HAP by first-principle method and using VASP in work [31] yielded the values which are very close to our data, second, that in work [32] the HAP surface charges density was experimentally measured by atomic force microscopy (AFM) using special functionalized tips. It turned out to have similar values.

3.2. Electronic and optical properties acting by defect energy levels in HAP

The most basic property of a periodic solid is its fundamental energy gap Eg= Ec – Ev (where Ec – is the conductive band bottom, Ev – is the valence band top), which is positive for semiconductors and insulators. This Eg dominates many properties. The fundamental energy gap of a periodic solid characterizes low-energy single-electron excitations. Band-gap problem in Kohn-Sham density functional theory is that the gap in the band-structure of the exact multiplicative Kohn-Sham (KS) potential substantially underestimates the fundamental gap. To avoid this problem the generalized KS theory (GKS) is developed, in which the band gap of an extended system equals the fundamental gap for the approximate functional if the GKS potential operator is continuous and the density change is de-localized when an electron or hole is added. In this case GKS band gaps from meta-generalized gradient approximations (meta-GGAs) and hybrid functionals can be more realistic than those from GGAs or even from the exact KS potential [25, 26].

For the case of one electron excitation, the following relations can be used: Ionization energy $I=E(+1)-E(0) = -E_v$, electron affinity $A=E(0)-E(-1)=-E_c$, and fundamental gap $E_g = I – A = E_c – E_v$, while the KS band edges are ε_{HO}, ε_{LU} (where the Highest Occupied (HO) and Lowest Unoccupied (LU) mark the corresponding electron energy states), and corresponding band gap is equal $\varepsilon_g = \varepsilon_{LU} - \varepsilon_{HO}$, in the PBE (step 1) and B3LYP (step 2) for calculations on the same 2x2x2 B3LYP lattice of HAP super-cell (HAP8). As a result, the values of magnitude $(I + A) / 2$, the energy difference from the gap centre to the vacuum level, depend only slightly on the approximation. For the case of our HAP $P6_3$ supercell model (in pristine bulk crystal), these relations computed using VASP [28], are presented in Table 2.

Defect HAP structures with oxygen vacancies V_O described above [26] were investigated in neutral, positive, and double positive charge states. For double positive charge states, new structures referred to as extended (or bridge) structures, were also found for the oxygen vacancy in HAP [26]. One type of extended structures can be described as a pair of neighbouring oxygen vacancies connected by O bridge, $2V_O + O$. A second type is described as a complex consisting of OH-vacancy next to an H-interstitial, $V_{OH} + H$. Two defects of type $2V_O + O$ are singled out and labelled $V_O(A)$ and $V_O(C)$. One $V_{OH} + H$ defect is referred to as $V_O(B)$. The structures types and stability of V_O defects strongly depend on the charge states [26]. For neutral and single positive cases, $V_O(I)-V_O(IV)$ are stable. For charge states, extended configurations $(V_O(A)-V_O(C))$ relax to $V_O(I)-V_O(IV)$ structures. If charges +2, structures $V_O(I)-V_O(IV)$ are unstable and relax to extended structures (see Fig.1).

Inspection of KS eigenvalues for k = Γ confirmed that V_O defects are all donors. Figure 3 shows the B3LYP Kohn-Sham (KS) energies of neutral vacancies V_O in the energy range of one-electron band gap $\epsilon_{cb} - \epsilon_{vb}$ = 7.34 eV ~ $\varepsilon_g = \varepsilon_{LU} - \varepsilon_{HO}$. Here, ϵ_{cb} and ϵ_{vb} are energies of the bottom and top of the conduction band and valence band, respectively, and correspond to KS band edges ε_{HO}, ε_{LU}. These are represented by solid horizontal

lines spanning the whole diagram width. The short horizontal lines represent the defect-related states, as obtained from the KS eigenvalues. Level occupation is indicated by upward and downward arrows. The value of ϵ_{cb} is the origin of the energy scale.

Although the Kohn−Sham band structure lacks any physical significance, we can always make use of Koopmans' theorem to connect the highest occupied state to the photoionization energy of the system under scrutiny [26]. With this in mind, it is evident that the simpler V_O(I)−V_O(IV) structures are deep donors with photoionization energies close to 6 eV, while semi-vacancy configurations (extended or bridge vacancy defects, which joined two molecular groups - see Fig. 1 d, e, f) are shallower donors, where promotion of electrons to the conduction band requires a low ionization energy. This makes these complex defects V_O(A)2+, V_O(B)2+, and V_O(C)2+ (with charge q=+2) rather stable species. (The details of its formations are given below).

As regards the cases of the oxygen vacancies V_O(I)−V_O(IV) with neutral charge q=0 and charge q=+1 (Fig.1, b, c), the same two-step DFT calculations of various defective HAP structures in our supercell model of hexagonal $P6_3$ group show that all the levels are double occupied by electrons

Table 2**.** Energy characterization of pristine bulk HAP8 (2x2x2) calculations in the main state.

Method	*(I + A)/2, eV*	*I= - E_v, eV*	*ε_{HO}, eV*	*A= -E_c, eV*	*ε_{LU}, eV*	*E_g, eV*	*ε_g , eV*
PBE	-4.598094	-1.979512	1.9801	-7.216676	7.2232	5.237165	5.2431
B3LYP	-4.395551	- 0.971008	0.7259	- 7.820094	8.0662	6.849086	7.3403

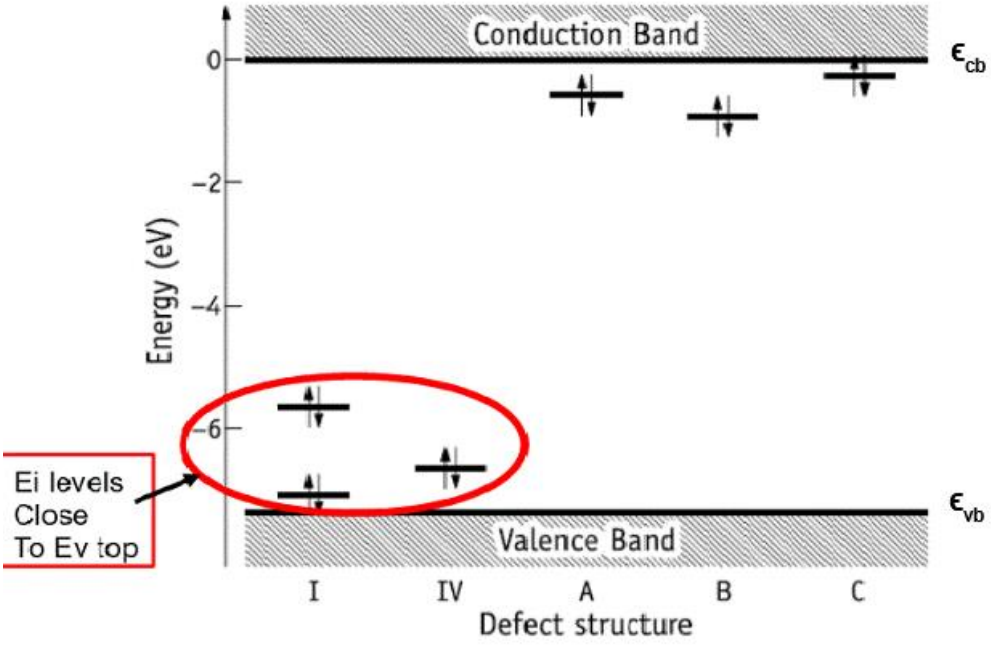

Figure 3. Kohn−Sham energy levels of neutral V_O defects in a HAP supercell at the k = Γ point. The defect structure I is also representative of structures II and III (see text). The latter have gap states that deviate from those of V_O(I) by less than 0.2 eV [26]. (Reprinted and modified with permission from [26]. Copyright (2019) American Chemical Society).

Table 3. Energy levels for A0 (V_O(I)−V_O(III) from 3 phosphate group) and D0 (V_O(IV) from hydroxyl group) (with double occupied by electron energy levels).

Defect	Method	$E_c = \varepsilon_{LU}$, eV	$E_v^* = \varepsilon^*_{HO}$, eV	$E_g = \varepsilon_{LU} - \varepsilon^*_{HO}$, eV	$E_i = \varepsilon_{HO}$, double occupied, eV	$E_{g\text{-}opt} = E_c - E_i$, eV	$E_i - E_v^*$, eV
A0 = A^0_I (V_O(I))	PBE	7.2208	2.1732	5.0476	3.3248	3.8960	1.1516
	B3LYP	8.0624	1.0127	7.0497	2.4418	5.6206	1.4291
A0 = A^0_{II} (V_O(II))	PBE	7.2231	2.0341	5.189	3.3606	3.8624	1.3265
	B3LYP	8.0640	0.8329	7.2311	2.4841	5.5799	1.6512
A0 = A^0_{III} (V_O(III))	PBE	7.2211	2.1049	5.1162	3.4816	3.7395	1.3767
	B3LYP	8.0619	0.9286	7.1333	2.6131	5.4488	1.6845
D0 = D^0 (V_O(IV))	PBE	7.2514	1.9646	5.2868	2.3930	4.8583	0.4284
	B3LYP	8.0946	0.7104	7.3842	1.4451	6.6495	0.7347

and all the data obtained for their KS energies are more close to the valence band top (these cases are presented in Table 3).

It must be noted that the energy of the highest occupied states in Figure 3 accounts for vertical transitions which are in principle accessible by optical excitation. However, transition levels (or electronic levels) of defects are equilibrium properties and must be derived from the formation energy of both ground states involved in the transitions. This is analogous to the zero-phonon (ZP) line energy in photo-luminescence/absorption experiments. Hence, the energy of a transition level of a defect will differ from the vertical (optical) transition by a Franck−Condon relaxation energy.

Usually the formation energy of a defect in a crystalline sample (with arbitrary volume) can be written as [33]:

$$E_f = E(q, R) - E_{HAP} - \sum_i \Delta n_i \mu_i + q(E_v + E_F) \quad (1)$$

which depends primarily on the energy difference between defective and pristine crystals, namely, E and E_{HAP}, respectively. The defect is considered on a particular configuration R and charge state q. The third and fourth terms account for any stoichiometric and charge imbalances between the first two terms. Accordingly, μ_i are chemical potentials for any species i which are respectively added ($\Delta n_i > 0$) or removed ($\Delta n_i < 0$) from or to the perfect crystal to make the defect. The last term accounts for the energy involved in the exchange of electrons between the defect in charge state q and an electron reservoir with a chemical potential $\mu_e = E_v + E_F$, where E_v and E_F stand for the energy of the valence band top and Fermi level, respectively. The latter mostly depends on the type and amount of defects and impurities in the crystal and can vary in the range $0 \le E_F \le E_g$, where E_g is the band gap width of the material.

This eq. (1) allows us to construct a phase diagram for the oxygen vacancy in HAP as a function of the chemical potentials and Fermi energy. In recent work [26] such calculations and analysis of the stability of some concrete species were carried out. It was shown that [26], the value of E_F, for which two solutions $E_f(q)$ and $E_f(q + 1)$ from eq. (1) become identical, defines a threshold above which V_O^q is more stable than V_O^{q+1}.

The defect transition level for two various charged states $E_f(q)$ and $E_f(q+1)$ can be calculated with respect to the valence band top E_V as

$$E(q/q+1) - E_V = [E(q, R^q) - E(q+1, R^{q+1})] - I_{bulk} \quad (2)$$

where different structures R^q and R^{q+1} have different charges q and q + 1, E is the total energy (including charge correction for $q \neq 0$), $I_{bulk} = E_{bulk}(q = +1) - E_{bulk}(q = 0)$ is the ionization energy of a bulk supercell.

One could have replaced I_{bulk} in (2) by the energy of the highest occupied KS energy level from a bulk calculation. We have chosen to avoid the use of Kohn−Sham energies, keeping the results solely based on total energies. The KS band gap from B3LYP-level calculations (E_g^{KS} = 7.34 eV) is about 0.49 eV wider than the quasi-particle gap (calculated as $E_g^{QP} = E_{bulk}(+1) + Eb_{ulk}(-1) - 2E_{bulk}(0)$ = 6.85 eV) [26].

In Table 4 the calculated transition levels, $\Delta E(q/q + 1) = E(q/q + 1) - E_V$ involving the relevant structures R^q and R^{q+1} are presented. Results based on both PBE and B3LYP functionals are reported. It is evident that PBE results have error bars of at least 1 eV, which is in line with our findings reported in [25].

As everyone can see, the position of these energy levels is not much different (especially for the PBE calculations), although in the case of B3LYP these levels are slightly higher than the E_v for the direct case. In any case, these deviations are within 1 eV.

It is also important to note that such levels close to the top of the valence band were recently observed by the photoelectron emission spectroscopy experiments, and the photoelectron work function from HAP was measured for different external actions [23, 34]. Moreover, it was noted in the work [34] that they may occur during a number of actions on HAP samples (heating and annealing, gamma irradiation, microwave effects and combined hydrogenation with microwave irradiations). It is in these cases that the formation of a sufficiently large number of oxygen vacancies is possible, especially in the OH group, with the lowest energies relative to the top of the valence band (see Tables 3 and 4).

Another important feature is the fact that single defects with positive charge are not stable. Considering the lowest energy structures for each charge state, it is possible to find that a transition level from q=0 to q=+2 (0/2+) is at the crossing point. The location of the level was calculated at $E(0/2+) - Ev = 2.65$ eV [26].

Hence, for p-type HAP, where the Fermi energy is at the lower-half of the gap, oxygen vacancies are likely to adopt double positive extended structures $V_O(B)^{2+}$ or $V_O(C)^{2+}$. Conversely, in n-type (and intrinsic) HAP, the neutral state is more stable and the defect will be found as an isolated H^- hydride in the OH-channel (i.e., $V_O(IV)^0$) [26].

Table 4**.** Calculated Electronic Donor Levels of V_O in HAp with Respect To the Valence Band top, $\Delta E(q/q + 1) = E(q/q+ 1) - E_v$. (Reprinted and adapted with permission from [26]. Copyright (2019) American Chemical Society.).

Functional	ΔE(0/+), eV	R^0/R^+	ΔE(+/2+), eV	R^+/R^{2+}
PBE	1.53	I/I	1.71	I/A
B3LYP	2.51		2.60	
PBE	1.58	II/II	2.64	II/B
B3LYP	2.50		3.74	
PBE	1.72	III/III	2.59	III/C
B3LYP	2.72		3.60	
PBE	0.17	IV/IV	3.08	IV/B
B3LYP	0.99		3.94	

Table 5. Main energy relations for HAP with D defects, when Oxygen vacancy is in OH (V_O(IV)), with Respect To the Conduction Band bottom $\Delta E(q/q+1) = Ec - [E(D^0)-E(D^+)]$, (all data are in eV units).

Method	$Ec - [E(D^0)-E(D^+)]$	$\Delta E(D^0/D^{0+}_{-1e}) = E(D^0) - E(D^{0+}_{-1e})$	E_{abs}	$E_{FC}(+)$	E_{lum}	$E_{FC}(0)$	$E_{abs} - E_{lum} = E_{FC}(+) + E_{FC}(0)$
PBE	4.927566	2.009449	5.207227	0.279661	3.379735	1.547831	1.827492
PBE on B3LYP lattice	5.071172	2.016323	5.200354	0.129182	3.518707	1.552465	1.681647
B3LYP	5.856286	1.963808	6.671180	0.814895	4.169527	1.686760	2.501654

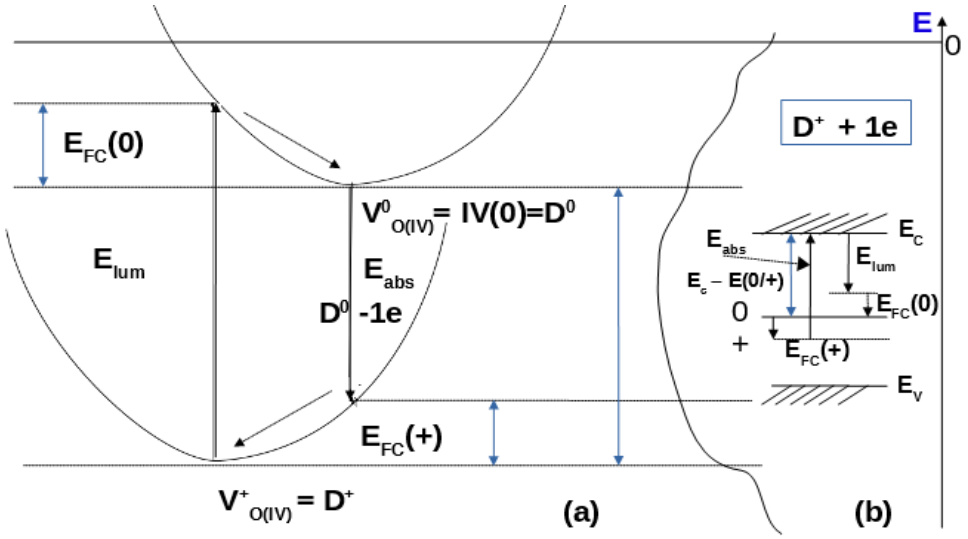

Figure 4. Schematics of the Franck-Condon relaxation processes: a) in direct energies changes during excitation / luminescence with corresponding lattice relaxation of atomic positions shifting; b) the corresponding energy band scheme with relation to E_C and E_V with $E_g = E_C - E_V$.

For Frank-Condon (FC) relaxation we must estimate the structure and energy changes during excitation/luminescence processes. In this case, similarly to eq. (2) we can calculate the defect transition level for two various charged states $E_f(q)$ and $E_f(q+1)$ with respect to the conduction band bottom E_C. By way of example we consider the case of V_O(IV) vacancy in our HAP $P6_3$ supercell model. In this case we can write

$$E_c - E(D^0/D^+) = A_b - [E(D^0) - E(D^+)] = A_{bulk} - [E(V_O^{q=0}(IV) - E(V_O^{q=+1}(IV)], \quad (3)$$

where $A_{bulk} = E_{bulk}(q = 0) - E_{bulk}(q = -1)$ is the electron affinity energy of a bulk supercell.

The main relaxation and processes in this case are shown in Fig. 4 and the data are presented in Table 5.

We must emphasize the difference between direct energy calculations from VASP data and the energies computed by relation (1) between energy of the defective and pristine crystals, with taken into account some stoichiometric and charge imbalances between them and the chemical potentials for any interacting species. As a result, the absorption and luminescence energies have

more correct values for solid states case. The relations obtained for FC relaxation in both cases (absorption and luminescence) have good and quite correct values for all approaches (see Table 5 last column).

4. CONCLUSIONS

Using various computational approaches developed we demonstrate that the ordered HAP hexagonal (space group $P6_3$) and monoclinic (space group $P2_1$) phases have strong own (spontaneous polarization) of the order of P_S ~ 0.05 – 0.15 C/m^2, which is determined by parallel orientation of the OH group dipoles (with some variations depending from structural and environmental conditions), while disordered hexagonal ad monoclinic phases have close to zero polarization P < 0.001 C/m^2, due to anti-parallel orientation of OH dipoles, that compensate one another. This behavior has a ferroelectric nature in whole. As a result, both ordered HAP phases have piezoelectric coefficients of the order of ~ 6.4 – 16.5 pm/V (which vary between these phases), and pyroelectric coefficients p ~ 10–100 mC/(m^{2}K), that are confirmed by many experimental data.

Optical properties of the defective HAP are determined by various defects formed by Oxygen vacancies, depending on charges state. Defect HAP structures with oxygen vacancies can be in neutral, positive, and double positive charge states. For double positive charge states new structures referred to as extended (or bridge) structures, were established in HAP.

We found that the vacancies essentially occur in such two distinct forms, either as a simple vacant oxygen site (referred to as structures I-IV), or as an oxygen atom replacing two neighbouring oxygen vacancies (bridge or extended structures named as “A-C”). The former type of vacancies is deep donors, while the latter are shallow donors with rather low ionization energies. No acceptor states (stable negatively charged defects) were found. Vacancy structures I-IV are more stable in the neutral charge state, while bridge structures A-C are preferred in the double plus charge state. This means that the oxygen vacancy adopts rather different configurations on samples where the Fermi energy is in the upper or the lower half of the band gap. From inspection of the one-electron Kohn-Sham levels, combined with the transition levels obtained from total energies, we find that electron promotion from the valence band top to the donor state of the positively charged structures, involves a zero-phonon absorption of 3.6-3.9 eV.

This transition leads to a spontaneous breaking of either a P-O bridge-bond or an O-H bond, and most likely explains the 3.4-4.0 eV absorption onset for the observation of photocatalysis under persistent UV illumination. The structure’s types and stability of defects strongly depend on the charge states. Inspection of the Kohn−Sham eigenvalues at k = Γ confirmed that neutral Oxygen vacancy defects are all donors involves the luminescence and absorption of 3.6−3.9 eV. This transition leads to a spontaneous breaking of either P−O−P or O−H−O bridge bonds on extended defects and most likely explains the 3.4−4.0 eV absorption onset for the observation of photocatalysis under persistent ultraviolet illumination.

Further development and more accurate calculation of these electronic properties and optical photoexciting and photocatalytic processes can be made by correct calculations of the electron-electron correlation of the excited electron states taking into account the Frank Condon relaxation. These contributions are calculated for the case of the V_O(IV) vacancy in our HAP $P6_3$ supercell model and their results showed that FC shift obtained has reasonable values (for electron excitation ~ 0.2 eV / 0.8 eV in PBE/B3LYP, and for luminescence ~1.6 eV / 1.8 eV in PBE/B3LYP). These investigations will be continued for other oxygen vacancy types.

However, we must conclude that for any case, irrespective of these FC relaxation processes, the formation of the various types defects in HAP through different oxygen vacancies gives rise to an opportunity of the photo-excitation processes in the close ultraviolet (UV-C) and visible light region. These photo-excitation effects obviously produce the photo-catalytic activity of HAP. One only needs to introduce a sufficient amount of these oxygen vacancies by some external actions, such as heating/annealing, gamma-irradiation and combined hydrogenation with microwave

irradiations [23]. In any case the electron photoexcitation from additional energy levels which arose due to oxygen vacancy inside the forbidden band gap can provide this photocatalityc activity of such treated HAP samples.

REFERENCES

[1] B. D. Ratner, A. S. Hoffman, F.J. Schoen, J.E. Lemons, *Biomaterials Science.* 3rd ed. Oxford: Academic Press, (2013).

[2] V. Bystrov, A. Bystrova, Yu. Dekhtyar, I. A. Khlusov, V. Pichugin, K. Prosolov, Yu. Sharkeev, Electrical functionalization and fabrication of nanostructured hydroxyapatite coatings. In: A. Iulian, eds. *Bioceramics and Biocomposites: From Research to Clinical Practice.* John Wiley & Sons, Inc., Hoboken, New Jersey, 149-190 (2019).

[3] B. Leon, J. A. Janson, *Thin calcium phosphate coatings for medical implants*. Berlin: Springer, (2009).

[4] M. Epple, K. Ganesan, R. Heumann, J. Klesing, A. Kovtun, S. Neumann and V. Sokolova, *J. Mater. Chem.* **20**, 18 (2010).

[5] M. I. Kay, R. A. Young, A. S. Posner, *Nature* **204**, 1050 (1964).

[6] S. Weiner, P. A. Price, *Calcif. Tissue Int.* **39**, 365 (1986).

[7] Noriko Kanzaki, Kazuo Onuma, Atsuo Ito, Kay Teraoka, Tetsuya Tateishi, Sadao Tsutsumi, *J. Phys. Chem. B.* **102**, 6471 (1998).

[8] V. S. Bystrov, *Math. Biol. Bioinform.* **12,** 14 (2017).

[9] C.A. Santana, C.Piccirillo, S.I.A. Pereira, R.C.Pullar, S.M.Lima, P.M.L. Castro, *Journal of Environmental Chemical Engineering.* **7**(5), 103403 (2019).

[10] N. Hitmi, C. LaCabanne, R. A. Young, *J. Phys. Chem. Solids*. **47 (**6), 533 (1986).

[11] S. Nakamura, H. Takeda, K. Yamashita, *J. Appl. Phys.* **89 (**10), 5386 (2001).

[12] S. A. M. Tofail, D. Haverty, K. T. Stanton, J. B. Mcmonagle, *Ferroelectrics.* **319**, 117 (2005).

[13] S. A. M. Tofail, D. Haverty, F. Cox, J. Erhart, P. Hána, V. Ryzhenko, *J. Appl. Phys.* **105**(6), 064103 (2009).

[14] S. A. M. Tofail, C. Baldisserri, D. Haverty, J. B. McMonagle, J. Erhart, *J. Appl. Phys.* **106**(10), 106104 (2009).

[15] S. B. Lang, S. A. M. Tofail, A. A. Gandhi, M. Gregor, C. Wolf-Brandstetter, J. Kost, S. Bauer, M. Krause, *Appl. Phys. Lett*. **98**, 123703 (2011).

[16] S. B. Lang, S. A. M. Tofail, A. L. Kholkin, M. Wojtaś, M. Gregor, A. A. Gandhi, Y. Wang, S. Bauer, M. Krause, A. Plecenik, *Sci. Rep*. **3**, 2215 (2013).

[17] S. B. Lang, *Phase transitions,* **89** (78), 678694 (2016).

[18] V.S. Bystrov, E. Paramonova, Yu. Dekhtyar, A. Katashev, A. Karlov, N. Polyaka, A.V. Bystrova, A. Patmalnieks, A.L. Kholkin, *J. Phys. Cond. Matter*. **23**, 065302 (2011).

[19] V.S. Bystrov, J. Coutinho, A.V. Bystrova, Yu.D. Dekhtyar, R.C. Pullar, A. Poronin, E. Palcevskis, A. Dindune, B. Alkan, C. Durucan, *J. Phys. D Appl. Phys.* **48**, 195302 (2015).

[20] V. S. Bystrov, *Ferroelectrics.* **475**, 148 (2015).

[21] V. S. Bystrov, *Ferroelectrics.* **541,** 25 **(**2019).

[22] H. Nishikawa, *Phosphorus Res. Bull*. **21**, 97 (2007).

[23] V.S. Bystrov, E.V. Paramonova, Yu.D. Dekhtyar, A. V. Bystrova, R.C. Pullar, S. Kopyl, D.M. Tobaldi, C. Piccirillo, L.A. Avakyan, J. Coutinho, *Ferroelectrics.* **509**, 105 (2017).

[24] V.S. Bystrov, C. Piccirillo, D.M. Tobaldi, P.M.L. Castro, J. Coutinho, S. Kopyl, R.C. Pullar, *Applied Catalysis B: Environmental*. **196**, 100 (2016).

[25] L.A. Avakyan, E.V. Paramonova, José Coutinho, Sven Öberg, V.S. Bystrov, Lusegen A. Bugaevet, *J. Chem. Phys.* **148**, 154706 (2018).

[26] V. S. Bystrov, L. A. Avakyan, E. V. Paramonova, J. Coutinho, *J. Chem. Phys.C.* **123**(8), 4856 (2019).

[27] AIMPRO, (2010). [http://aimpro.ncl.ac.uk/] (Accessed February 2016).

[28] VASP (Vienna Ab initio Simulation Package), [https://www.vasp.at/] (Accessed July 2019).

[29] HyperChem:Tools for Molecular modeling (release 8). Gainnesville: Hypercube, Inc. 2002.

[30] C. Halperin, S. Mutchnik, A. Agronin, M. Molotskii, P. Urenski, M. Salai, G. Rosenman, *Nano Lett.,* **4** (7), 1253 (2004).

[31] Shunbo Hu, Fanhao Jia, Cornelia Marinescu, Fanica Cimpoesu, Yuting Qi, Yongxue Tao, Alessandro Stroppa, Wei Ren, *RCS Adv.*, **7**, 21375 (2017).

[32] Jennifer Vandiver, Delphine Dean, Nelesh Patel, William Bonfield, Christine Ortiz, *Biomaterials*. **26**, 271 (2005).

[33] G.-X. Qian, R. M. Martin, D. J. Chadi, *Phys. Rev. B: Condens. Matter Mater. Phys.* **38**, 7649 (1988).

[34] A. V. Bystrova, Yu. Dekhtyar, A. I. Popov, , J. Coutinho, V.S. Bystrov, *Ferroelectrics* **475**(1), 135 (2015).

[35] V. Bystrov, A. Bystrova, Yu. Dekhtyar, *Advances in Colloid and Interface Science* **249**, 213 (2017).

NANOMATERIALS SCIENCE & ENGINEERING
Vol. 1, No. 1, pp. 22-29 (2019)

RESEARCH ARTICLE

https://proa.ua.pt/index.php/nmse/

Mechanical properties of polypropylene biocomposites with sea weeds

Munir Tasdemir

Marmara University, Technology Faculty, Metallurgy and Materials Eng. Dep., Istanbul, 34722, Turkey
e-mail address: munir@marmara.edu.tr

Received 16 October 2019; accepted 2 December 2019; published online 19 December 2019

ABSTRACT

The interest in the utilization of bio fillers in thermoplastics has increased recently, mainly due to the need in overcoming the environmental problems caused by the agricultural by products. Based on former exploratory research, we used seaweed fiber as a novel bio filler for the production of polypropylene (PP) biocomposites. Maleic anhydride grafted PP was applied as compatibilizers. The incorporation of the bio fillers at compositions ranging from 10-30% was carried out by melt compounding in extruder and then injection moulded into standard test samples. Mechanical and physical characteristics of the composite systems were studied to evaluate the effect of seaweeds content on PP. It has been found that while there is a decrease in elasticity modulus, tensile strength at break and elongation etc., the hardness and melt flow index were found to be increased with the seaweed content.

1. INTRODUCTION

Polymer/natural fiber biocomposites have recently drawn great attentions in fundamental research and industrial applications for their ecological and economic advantages. Besides environmental concerns, natural fiber reinforced polymer biocomposites provide a unique combination of high performance, great versatility, and processing advantages at favorable costs. Natural lignocellulosic fibers are renewable, completely or partially recyclable and biodegradable; flax, cotton, hemp as well as wood fiber are applied as bio fillers into polymeric matrices [1-4]. Their significant weight saving, low cost and other advantages promote natural fibers as ideal alternative fillers to glass and carbon fibers. Natural fiber biocomposites have already appeared in industrial scale as furniture, household appliances, and as automotive materials [5]. The most important disadvantage of such composite materials is the problem of disposal after end use. This raised the attention of people for the use of natural, sustainable, biodegradable and renewable resources. In modern production environment, there is a great demand for every material to be recyclable or degradable.

Polypropylene is an outstanding commercially available important thermoplastic material with wide range of applications in various fields because of its balanced chemical and mechanical properties [6, 9]. Natural fiber composites, are composite materials i.e., formed by a matrix (resin) and a reinforcement (fiber), in which the fibers are natural i.e., mainly formed by cellulose and therefore originating from plants and bacteria. Some of these fibers can be hemp, jute, flax, sisal, banana, kapok, corn husk etc. [6-10].

Satisfying mechanical properties of different polymer/ natural fiber biocomposites have been reported. Natural fibers have successfully enhanced polymeric matrices with and even without compatibilizers at different natural fiber loadings [11-13]. Thermal properties of

lignocellulosic biocomposites are also of great importance. Remarkable promotion of crystallinity of polymer matrix by natural fibers was reported.

The present work is aimed at the following objectives. To use sea weeds as bio fillers at different composition in polypropylene to get biocomposite and to determine its effect on mechanical, physical and morphological properties of polypropylene bio-composites.

2. EXPERIMENTAL

2.1. Compositions and Materials

Seven different polymer composites were prepared. Compositions of polypropylene/seaweed/maleic anhydride grafted polypropylene (PP/SW/MAPP) polymer composites that were formed are given in Table 1. PP (Moplen EP 3307) supplied by Lyondell Basell. Its density is 0.900 g/cm^3, MFI value is 15 g/10 min (230 ^{o}C, 2,16 Kg) and its head deflection temperature (0.45 MPa, unannealed) is 95.0 ^{o}C. Seaweed was collected from the Cape peninsula coastal region near Cape Town (South Africa) which was washed with water and dried.

2.2. Sample Preparation

The sea weed was washed thoroughly with water to remove the adhered contaminants, and dried in an air oven at 105^{0}C for 24 hours. The size of seaweed particles varied between 30-250 microns. Powder preparation steps are given in Figure 1. Polypropylene, seaweed and maleic anhydride grafted polypropylene were dried overnight at 105 ^{o}C for 24 h in a vacuum oven prior to melt blending. Mechanical premixing of solid compositions was done using a LB-5601 liquid-solids blender (The Patterson-Kelley Co., Inc.USA) brand batch blender for 20 min. Samples with various proportions of PP/SW/MAPP polymer composites were produced between 190-225 ^{o}C at 17 bar pressure, and a rotation rate of 28 rpm, with a Microsan extruder (Microsan Instrument Inc. Turkey). The extruded was cooled and pelletized into granules and dried in vacuum oven at 105 ^{o}C for 24 hours. Subsequently, test samples were manufactured by injection molding. Injection temperature was 190-225 ^{o}C, pressure was 100-120 bar and screw speed was 28 rpm.

Table 1. Composition of the PP/SW/MAPP polymer composites formulations.

Groups	PP (wt %)	Seaweeds (wt %)	MAPP (wt %)
1	100	-	-
2	90	10	-
3	80	20	-
4	70	30	-
5	90	10	5
6	80	20	5
7	70	30	5

waste granulation powder

Figure 1. Seaweed powder preparation steps.

2.3. Test Procedure

The elasticity modulus, yield strength, tensile strength at break and % elongation of the compressed plates were measured by using a tensile testing machine (Zwick Z010, Germany) according to ASTM D638 at room temperature and crosshead speed of 50 mm/min. For every composition, seven samples were tested. The hardness test was done according to the ASTM D2240 method with Zwick hardness tester. To investigate fracture behavior, Izod impact test (notched) was done at room temperature according to the ASTM D256 method with Zwick B5113 impact tester (Zwick, Germany). Heat deflection temperature (HDT) and Vicat softening point tests were done according to ISO 75 and ISO 307 standard with determined by CEAST 6521. HDT-Vicat test equipment. Flow behavior testing of all the mixtures was done according to ISO 1133 standard with Zwick 4100 MFI equipment. The fractured surfaces of the PP/SW/MAPP polymer composites were coated to thickness of 20 Å of a gold (Au) to prevent electrical charging by Polaron SC7640 (high resolution sputter coater) (United Kingdom). The surfaces of the prepared samples were observed by the FEI Sirion XL30 FEG (Nederland) scanning electron microscopy (SEM) at an acceleration voltage of 10 and 20 kV.

3. RESULT AND DISCUSSION

3.1. Mechanical properties of seaweed filled PP

The relationship between the elasticity modulus and the percentage of the seaweed of PP composites is shown in the Figure 2-A. With inclusion of seaweed particles in the polymer matrix the elasticity modulus of the composite is found to be decreasing. For example, the elasticity modulus of the three different samples (with 10, 20, and 30 wt% of seaweed, without MAPP) is measured as 571, 530, and 424 MPa respectively. The elasticity modulus of pure PP is 550 MPa. In comparison with the elasticity modulus of virgin PP, the elasticity modulus decreased by 23% for the composites with a 30 wt % seaweed concentration. On the other hand, the elasticity modulus of the three different samples (with 10, 20, and 30 wt% of seaweed, with 5% MAPP) is measured as 545, 512, and 396 MPa respectively. In comparison with the elasticity modulus of virgin PP, the elasticity modulus decreased by 23% for the composites with a 30 wt % seaweed concentration. MAPP addition reduced elastic modulus value, possibly due to poor compatibilisation of seaweeds in the PP matrix.

N. Jaya Chitra et al. [14] investigated polypropylene/seaweed biocomposites and they found similar results. For example, tensile modulus of biocomposites decreased with increasing seaweed rate. The relationship between the yield strength and the percentage of the seaweed of PP composites is shown in the Figure 2-B. With inclusion of seaweed particles in the polymer matrix the yield strength of the composite is found to be decreasing. For example, the yield strength of the three different samples (with 10, 20, and 30 wt% of seaweed, without MAPP) is measured as 22, 21, and 18 MPa respectively. The yield strength of pure PP is 29 MPa. In comparison with the yield strength of virgin PP, the yield strength decreased by 40% for the composites with a 30 wt % seaweed concentration. On the other hand, the yield strength of the three different samples (with 10, 20, and 30 wt% of seaweed, with 5% MAPP) is measured as 23, 22, and 22 MPa respectively. In comparison with the yield strength of virgin PP, the yield strength decreased by 24% for the composites with a 30 wt % seaweed concentration. The relationship between the tensile strength at break and the percentage of the seaweed of PP composites is shown in the Figure 2-C. With inclusion of seaweed particles in the polymer matrix the tensile strength at break of the composite is found to be decreasing. For example, the tensile strength at break of the three different samples (with 10, 20, and 30 wt% of seaweed, without MAPP) is measured as 14, 13, and 12 MPa respectively. The tensile strength at break of pure PP is 19 MPa. In comparison with the tensile strength at break of virgin PP, the tensile strength at break decreased by 37% for the composites with a 30 wt % seaweed concentration. On the other hand, the tensile strength at break of the three different samples (with 10, 20, and 30 wt% of seaweed, with 5% MAPP) is measured as 16, 14, and 13.5 MPa respectively. In comparison with the tensile

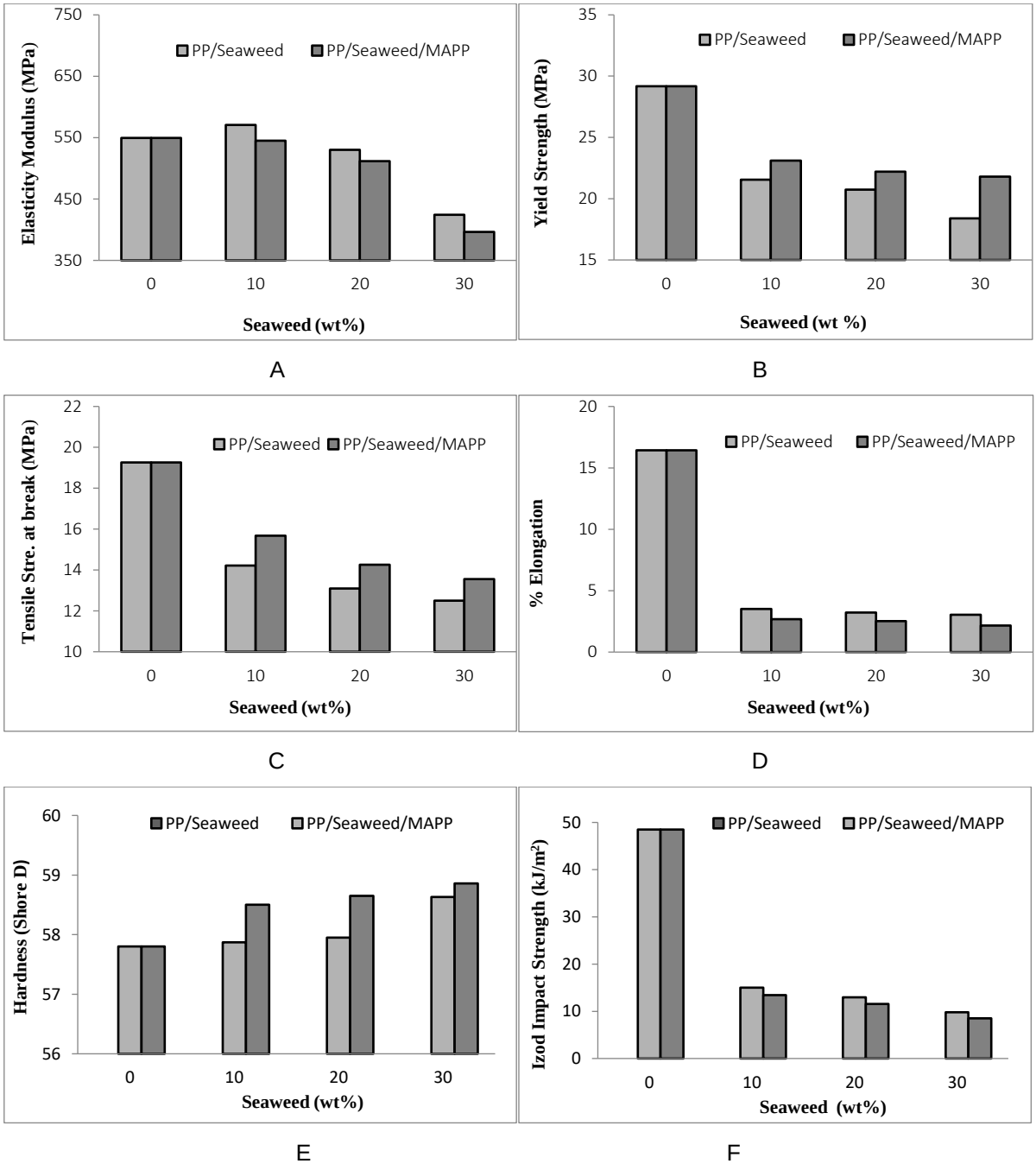

Figure 2. Mechanical properties of PP/SW/MAPP polymer composites.

strength at break of virgin PP, the tensile strength at break decreased by 31% for the composites with a 30 wt % seaweed concentration. Lixing Luan et al. [15] investigated polypropylene/seaweed biocomposites and they found similar results. For example, tensile strength at break values of biocomposites decreased with increasing seaweed rate. N. Jaya Chitra et al. [14] investigated polypropylene/seaweed biocomposites and they found similar results. For example, tensile strength

at break values of biocomposites decreased with increasing seaweed rate. The relationship between the % elongation and the percentage of the seaweed of PP composites is shown in the Figure 2-D. With inclusion of seaweed particles in the polymer matrix the % elongation of the composite is found to be decreasing. The % elongation of the three different samples (with 10, 20, and 30 wt% of seaweed, without MAPP) is measured as 4, 3, and 3 % respectively. The % elongation of pure PP is 16 %. In comparison with the % elongation of virgin PP, the % elongation decreased by 81% for the composites with a 30 wt % seaweed concentration. On the other hand, the % elongation of the three different samples (with 10, 20, and 30 wt% of seaweed, with 5% MAPP) is measured as 3, 2.5, and 2 % respectively. In comparison with the % elongation of virgin PP, the % elongation decreased by 87.5% for the composites with a 30 wt % seaweed concentration. N. Jaya Chitra et al. [14] investigated polypropylene/seaweed biocomposites and they found similar results. For example, % elongation values of biocomposites decreased with increasing seaweed rate. The relationship between the hardness and the percentage of the seaweed of PP composites is shown in the Figure 2-E. With inclusion of seaweed particles in the polymer matrix the hardness of the composite is found to be a little increasing. For example, the hardness of the three different samples (with 10, 20, and 30 wt% of seaweed, without MAPP) is measured as 57.87, 57.95, and 58.63 Shore D respectively. The hardness of pure PP is 57.8 Shore D. In comparison with the hardness of virgin PP, the hardness increased by 1.4% for the composites with a 30 wt % seaweed concentration. On the other hand, the hardness of the three different samples (with 10, 20, and 30 wt% of seaweed, with 5% MAPP) is measured as 58.5, 58.65, and 58.86 Shore D respectively. In comparison with the hardness of virgin PP, the hardness increased by 1.7% for the composites with a 30 wt % seaweed concentration. The relationship between the Izod impact strength and the percentage of the seaweed of PP composites is shown in the Figure 2-F. With inclusion of seaweed particles in the polymer matrix the Izod impact strength of the composite is found to be decreasing. For example, the Izod impact strength of the three different samples (with 10, 20, and 30 wt% of seaweed, without MAPP) is measured as 15, 12.96, and 9.8 kJ/m^2 respectively. The Izod impact strength of pure PP is 48.48 kJ/m^2. In comparison with the Izod impact strength of virgin PP, the Izod impact strength decreased by 79% for the composites with a 30 wt % seaweed concentration. On the other hand, the Izod impact strength of the three different samples (with 10, 20, and 30 wt% of seaweed, with 5% MAPP) is measured as 13.45, 11.53, and 8.54 kJ/m^2 respectively. In comparison with the Izod impact strength of virgin PP, the Izod impact strength decreased by 82% for the composites with a 30 wt % seaweed concentration.

3.2 Physical properties of the seaweed filled PP

The relationship between the Vicat softening point and the percentage of the seaweed of PP composites is shown in the Figure 3-A. With inclusion of seaweed particles in the polymer matrix the Vicat softening point of the composite is found to be decreasing. For example, the Vicat softening point of the three different samples (with 10, 20, and 30 wt% of seaweed, without MAPP) is measured as 131, 126, and 119 ^{o}C respectively. The Vicat softening point of pure PP is 134 ^{o}C. In comparison with the Vicat softening point of virgin PP, the Vicat softening point decreased by 11% for the composites with a 30 wt % seaweed concentration. On the other hand, the Vicat softening point of the three different samples (with 10, 20, and 30 wt% of seaweed, with 5% MAPP) is measured as 133.5, 130.7, and 122.6 ^{o}C respectively. In comparison with the Vicat softening point of virgin PP, the Vicat softening point decreased by 8.5% for the composites with a 30 wt % seaweed concentration. MAPP addition reduced Vicat softening point value. The relationship between the HDT and the percentage of the seaweed of PP composites is shown in the Figure 3-B. With inclusion of seaweed particles in the polymer matrix the HDT of the composite is found to be decreasing.

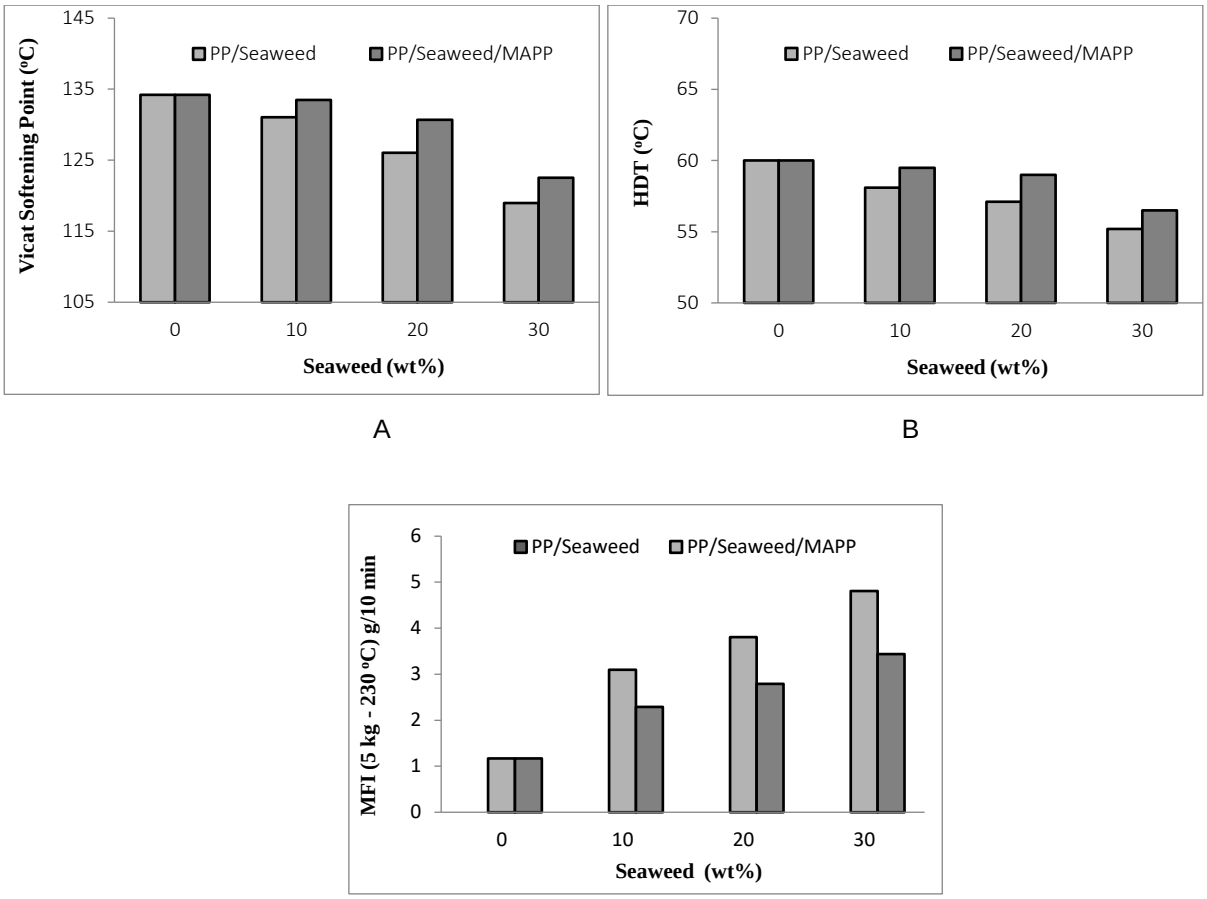

Figure 3. Physical properties of PP/SW/MAPP polymer composites.

For example, the HDT of the three different samples (with 10, 20, and 30 wt% of seaweed, without MAPP) is measured as 58.1, 57.1, and 55.2 °C respectively. The HDT of pure PP is 60 °C. In comparison with the HDT of virgin PP, the HDT decreased by 8% for the composites with a 30 wt % seaweed concentration. On the other hand, the HDT of the three different samples (with 10, 20, and 30 wt% of seaweed, with 5% MAPP) is measured as 59.5, 59, and 56.5 °C respectively. In comparison with the HDT of virgin PP, the HDT decreased by 5.8% for the composites with a 30 wt % seaweed concentration. The relationship between the MFI and the percentage of the seaweed of PP composites is shown in the Figure 3-C. With inclusion of seaweed particles in the polymer matrix the MFI of the composite is found to be increasing. For example, the MFI of the three different samples (with 10, 20, and 30 wt% of seaweed, without MAPP) is measured as 3.1, 3.8, and 4.8 g/10 min respectively. The MFI of pure PP is 1.2 g/10 min. In comparison with the MFI of virgin PP, the MFI increased by 300% for the composites with a 30 wt % seaweed concentration. On the other hand, the MFI of the three different samples (with 10, 20, and 30 wt% of seaweed, with 5% MAPP) is measured as 2.3, 2.8, and 3.4 g/10 min respectively. In comparison with the MFI of virgin PP, the MFI increased by 183% for the composites with a 30 wt % seaweed concentration.

3.3 Morphological properties of the seaweed filled PP

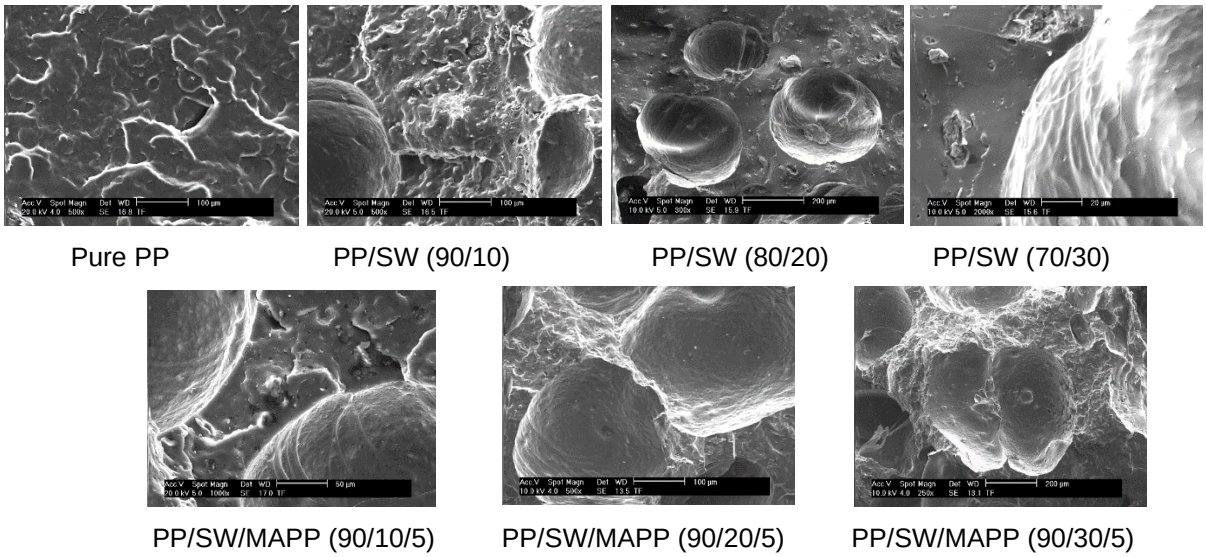

Figure 4. SEM photographs of PP/SW/MAPP polymer composites.

The SEM study was carried out to study the dispersion of SW in the PP matrix. Scanning electron microscopic observation is considered as an effective method for accessing visibility between the components in a polymer blend. The boundaries and the contrast can be obviously seen between the SW and PP matrix on the fractured surfaces of polymer matrix (Figure 4). The micrographs indicate that the all SW particulates are homogeneously dispersed on the fractured surfaces of polymer matrix.

4. CONCLUSIONS

The effects of seaweed and maleic anhydride grafted PP on the some properties, the elastic modulus, yields strengths, tensile strengths, % elongation, hardness, Izod impact resistance, Vicat softening point, HDT, MFI and morphological of PP/SW/MAPP composites were investigated. Seaweed a waste can be used as a potential filler material in polypropylene matrix composites. It has effects on the mechanical properties of the composites. The following results were obtained: The elasticity modulus, yield strength, tensile strength at break and % elongation of PP/SW/MAPP composites decreased as the seaweed concentration increases. The hardness of PP just a little increased as the seaweed concentration increases from 0 to 30 wt %. On the other hand, Izod impact strength of composites decreased as the seaweed concentration increases from 0 to 30 wt %. The micrographs indicate that the seaweed particulates are homogeneously dispersed on the fractured surfaces of PP matrix.

ACKNOWLEDGMENTS

This work has been supported by the Scientific Research Project Program of Marmara University (FEN-D-130319-0077)

REFERENCES

[1] E. Bodros, C. Baley, *Mater Lett* **62**, p.2143,(2008).
[2] M. A. Mydul, A. Toufiq, H. Monimul, *Polym. Plast. Technol. Eng.* **48**, 110 (2008).
[3] G. Sui, M. A. Fuqua, C.A. Ulven, W. H. Zhong, *Bioresource Technol* **100**, 1246 (2009).
[4] S. V Joshi, L. T. Drzal, A. K Mohanty, S. Arora, *Compos* **Part A 35-3**, 371 (2004).
[5] A. Gomesa, T. Matsuoa, K. Godab, J. Ohgi, *Compos* **Part A 38**, 1811 (2007).
[6] N. Hatta, N. Akmar, CUTSE International Conference 24-27 November (2008) Malaysia.
[7] B.S. Ndazi, C. Nyahumwa, Tesha , *J. Bio Resources* **3(4)**, 1267 (2007)
[8] A.S.Murtuza, International Conference on Advances in Polymer Technology, Feb 26-27, (2010) India, pp.60
[9] M. Shahril Ezuan Mustapa, Azman Hassan and Abdul Razak Rahmat, Simposium Polimer Kebangsaan Ke-V. Ogos 23-24, (2005)
[10] J. Wang, J.Tavakoli, Y. Tang, *Carbohydrate Polymers* **219**, 63 (2019).
[11] P. A. Sreekumar, P. Albert, G. Unnikrishnan, K. Josepy, S. Thomas, *J. Appl. Polym. Sci.* **109**, 1547 (2008).
[12] A. M. S. Silva, K. G. K. Fermoseli, M.A.D. Paoli, *J. Appl. Polym. Sci* .**112**, 3686 (2009).
[13] A. S. Shigha, KV.K. Thakur, *Polym. Plast. Technol. Eng* **48**, 201 (2009).

[14] N. J. Chitra, R.V. Kumari, *Research Journal of Pharmaceutical, Biological and Chemical Science*, **3**(3), 1165 (2012)

[15] L. Luan, W. Wu, M.H. Wagner, M. Mueller, *J. of Applied Polymer Science*, **118**, 997 (2010).

NANOMATERIALS SCIENCE & ENGINEERING
Vol. 1, No. 1, pp. 30-33 (2019)

RESEARCH ARTICLE

https://proa.ua.pt/index.php/nmse/

Crystal growth modes and crystallization kinetics of amorphous films according to transmission electron microscopy "in situ"

Aleksandr Bagmut and Ivan Bagmut

National Technical University "Kharkiv Polytechnic Institute"
NTU "KhPI" 2, Kyrpychova str., 61002, Kharkiv, Ukraine
e-mail address: bagmut@kpi.kharkov.ua

Received 16 October 2019; accepted 2 December 2019; published online 19 December 2019

ABSTRACT

The generality of the processes of crystal growth from the vapor phase on substrate and from the amorphous state in films is that in both cases a disorder-order transition takes place. This predetermines the structural and morphological analogy between the main forms of crystal growth on substrates and the main types of crystallization of amorphous films. Based on the analysis of the structure and morphology of crystals growing in amorphous films at electron beam influence, a quantitative interpretation of layer polymorphous crystallization (analog of Frank-van der Merwe growth mode), island polymorphous crystallization (analog of Volmer–Weber growth mode) and dendrite polymorphous crystallization (analog of Stranski–Krastanov growth mode) where given. For each crystallization mode the parameter of dimensionless relative length δ_0, equal to the ratio of the characteristic length to the value, characterizing the size of the unit cell of the crystal, were assigned and crystallization curves were built.

1. INTRODUCTION

Physical disturbance on the amorphous film can initiate its crystallization. If this is the disturbance of an electron beam, then we are talking about electron-beam crystallization, which can be performed in a transmission electron microscope column, using the so-called "in situ" method [1]. The phenomenological scheme of the transformations amorphous-crystal film suggests the following modes [2, 3]. 1. Layer polymorphous crystallization (LPC), when the inequality $\sigma_a \geq \sigma_c+\sigma_{ac}+\varepsilon_d$ is satisfied. Here σ_a, σ_c, σ_{ac} are the surface energy of amorphous phase-vacuum interface, of the crystalline phase-vacuum interface and surface energy of the amorphous-crystalline phase interface respectively. ε_d is the energy of deformation of the growing crystalline layer. 2. Island polymorphous crystallization (IPC), when the opposite inequality $\sigma_a \leq \sigma_c+\sigma_{ac}+\varepsilon_d$ is satisfied. 3. Dendrite polymorphous crystallization (DPC), when initially $\sigma_a \geq \sigma_c+\sigma_{ac}+\varepsilon_d$, and after critical dimension of a crystal, when $\sigma_a \leq \sigma_c+\sigma_{ac}+\varepsilon_d$.

The aim of this work was to give an overview of kinetics and types of crystallization of amorphous films, obtained predominantly by laser evaporation.

2. EXPERIMENTAL

Laser erosion plasma was deposited on substrates of KCl (001) at room temperature. Sputtering of a target (Cr, V, Zr, Hf) was carried out in an oxygen atmosphere ($P(O_2)$ ~ 0.13 Pa) with the use of a radiation from an LTI-PCh-5 laser operating in the Q-switched mode. The thickness of the films varied in the range from 20 to 35 nm. Crystallization of films was initiated by electron beam irradiation in

the column of a transmission electron microscope at a beam current of ~ 20 μA. The rate of crystallization was controlled by varying the density *j* of the electron current through the sample, which was varied in the range from 1.1 to 6.5 A·mm^{-2} depending on the electron beam focusing.

The structural analysis was carried out by the methods of electron diffraction and transmission electron microscopy on EM-100L and PEM-100-01 electron microscopes operating at an accelerating voltage of 100 kV. The process of crystallization of a film was recorded from the screen of an electron microscope with a Canon Power Shot G15 camera in the video recording mode at a frame rate of 30 s^{-1}. Data on the kinetics of the crystallization process were obtained from the analysis of individual frames of the video recorded “in situ” at a fixed electron current density.

Quantification of the crystallization type (LPC, IPC ore DPC) was carried out on the basis of the value of relative length δ_0, defined as

$$\delta_0 = \frac{D_0}{a_0} \quad (1)$$

in the case of LPC, and as

$$\delta_0 = \frac{D_0}{\sqrt[3]{\Omega}} \quad (2)$$

in the case of IPC and DPC. Characteristic unit of length D_0 is average crystal size at a moment of characteristic unit of time t_0, after which the volume of the amorphous phase decreases by a factor of e = 2.718 [4,5]:

$$D_0 = vt_0. \quad (3)$$

In expression (1) a_0 is a cell parameter of a growing crystal. In expression (2) Ω is the volume of the unit cell of a growing crystal. In expression (3) v is the crystal growth rate. The difference in the determination of δ_0 is due to the fact, that in the case of LPC a single crystal (with a cell parameter a_0) is formed in the investigated region, and in the case of IPC and DPC a polycrystalline film whose grains have different orientations [3, 6].

3. RESULTS AND DISCUSSION

Fig. 1a shows the mode of LPC of amorphous film of Cr_2O_3. A contrast extinction contour indicates to a dome-like bend of a crystal due to the tensile action of amorphous matrix. The dependence of the disk diameter $D(t)$ of the crystal and of the fraction of the crystalline phase $x(t)$ on time t are shown in Fig. 2a and 2b respectively. According to Fig. 2a the crystal growth rate $v=D'_t \approx 1.434$ μm·s^{-1}. There is a quadratic dependence $x(t)=1.276\ t^2$. So, characteristic unit of time $t_0 = 0.704$ s. According to (3) characteristic unit of length $D_0 = v \cdot t_0 = 1.01$ μm. For the (001) Cr_2O_3 orientation the projection of the unit cell on the plane of the film is a rhomb with a side $a_0 = 0.496$ nm. In this case, according to (1), the relative length $\delta_0 = D_0/a_0 \approx 2036$.

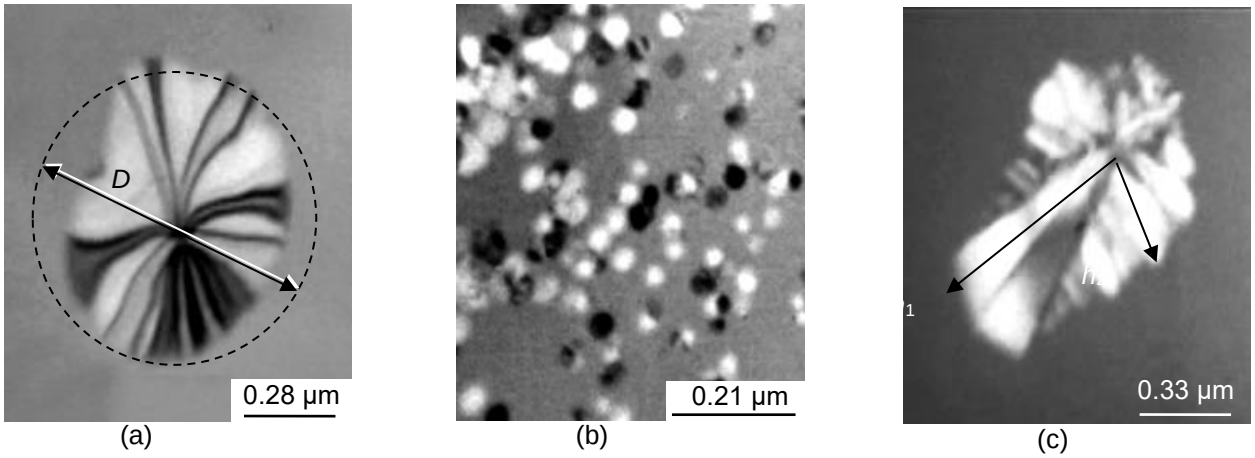

Figure 1. Crystal growth modes at electron beam effects on amorphous film. a - layer polymorphous crystallization of Cr_2O_3. b - island polymorphous crystallization of ZrO_2. c - dendrite polymorphous crystallization of HfO_2.

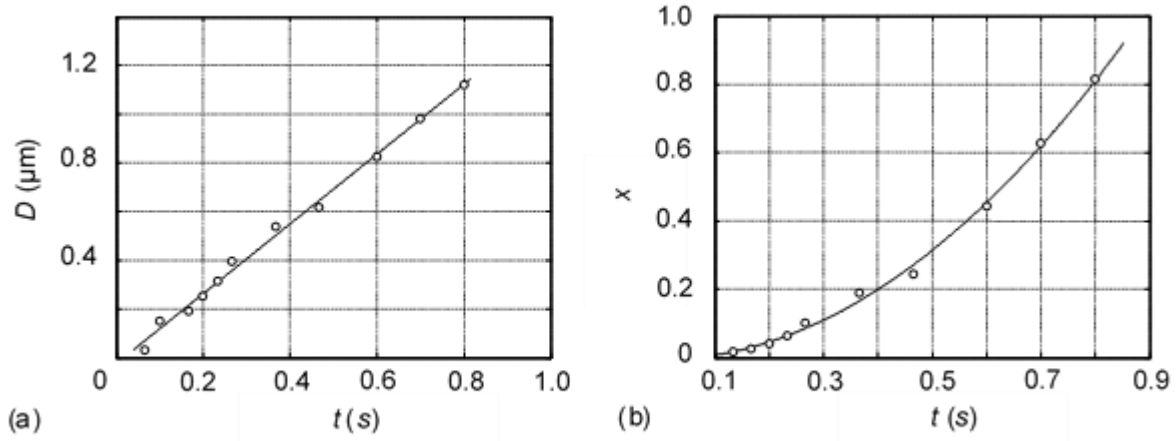

Figure 2. Kinetics of layer polymorphous crystallization of Cr_2O_3. a - The dependence of the diameter of the crystal *D*(t). b - The dependence of the fraction of the crystalline phase *x*(*t).*

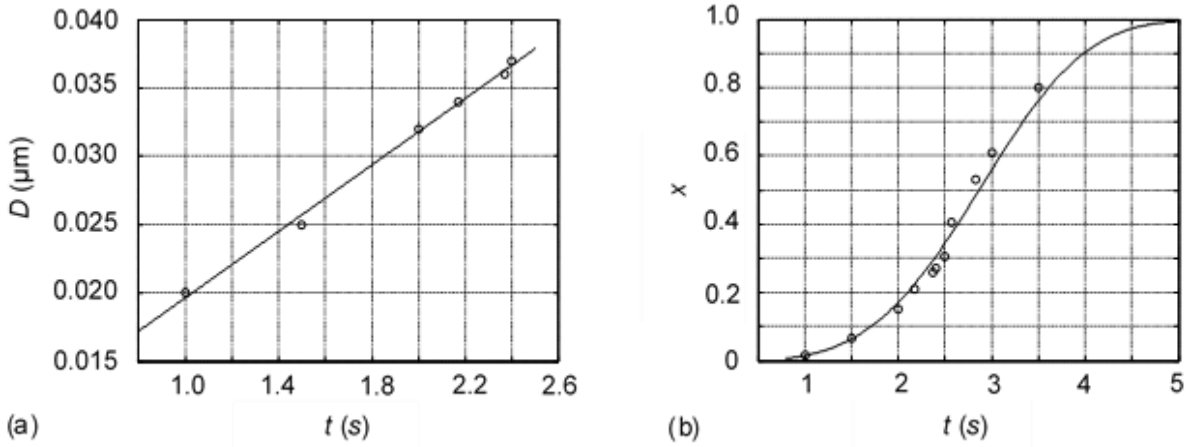

Figure 3. Kinetics of island polymorphous crystallization of ZrO_2. a - The dependence of the average iameter of the crystal *D*(t). b - The dependence of the fraction of the crystalline phase *x*(*t).*

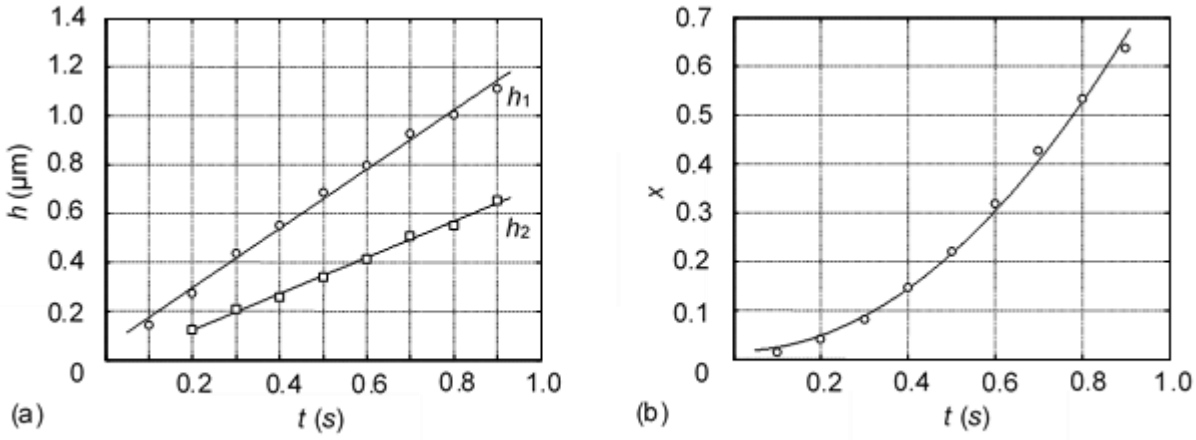

Figure 4. Kinetics of dendrite polymorphous crystallization of HfO_2. a - The dependence of the dendrite branches length h_1 and h_2 on time *t*. b - The dependence of the fraction of the crystalline phase *x*(*t).*

Fig. 1b shows the mode of IPC of amorphous film of ZrO_2. The dependence of the average diameter $D(t)$ of the crystals and of the fraction of the crystalline phase $x(t)$ on time t are shown in Fig. 3a and 3b respectively. According to Fig. 3a, the growth rate of the average diameter of the crystals $v = D'_t \approx 0.012$ μm·s^{-1}. There is exponential dependence $x(t)=1-\exp(-0.015t^{3.6})$. So, characteristic time $t_0=3.211$ s and characteristic length $D_0=v\cdot t_0=0.039$μm. The volume of ZrO_2 cubic sell $\Omega=1.32\cdot10^{-10}$μm^3. In this case, according to (2) the relative length $\delta_0=D_0/\Omega^{⅓} \approx 77$. The smaller the grain size of the crystallized film, the smaller the relative length δ_0.

Fig. 1c shows the mode of DPC of amorphous film of HfO_2. The dependence of the dendrite branches length h_1 and h_2 on time t is shown in Fig. 4a. According to Fig. 4a the growth rate of the dendrites branches of the first order $v_1 = (h_1)'_t \approx 1.215$ μm·s^{-1} and of the second order $v_2 = (h_2)'_t \approx 0.744$ μm·s^{-1}. The smaller the dendrite branch order, the smaller its growth rate. According to Fig. 4b takes place a quadratic dependence $x(t) = 0.799\ t^2$. So, characteristic time $t_0 = 0.889$ s and characteristic length $D_0 \approx 2v_1t_0 \approx 2.160$ μm. The volume of HfO_2 monoclinic sell $\Omega=1.38\cdot10^{-10}$μm^3. In this case, according to [2], the relative length $\delta_0=D_0/\Omega^{⅓} \approx 4180$.

4. CONCLUSION

Data of this work and of the literature [6, 7] show, that typical value of δ_0 are several thousand for LPC and DPC, and several hundreds for IPC. The dependence $x(t)$ is quadratic for layer and dendrite polymorphic crystallization, and exponential one for island polymorphic crystallization.

The generality of the processes of crystal growth from amorphous state and from the vapor state is that in both cases a disorder-order transition takes place. It is natural to compare the formation of a single crystal layer in amorphous film (mode of LPC) to the formation of a single crystal layer on substrate during vapor condensation (layer-by-layer growth), that corresponds to Frank-van der Merwe growth mode [8]. According to Bauer's criterion [8], this mode is realized when the inequality $\gamma_s \geq \gamma_f+\gamma_{sf}$ is satisfied. Here γ_s, γ_f, γ_{sf} are the surface energy of substrate, film, and interphase energy between the film and substrate, respectively. Formation of a polycrystalline layer in amorphous film (mode of IPC) correspond to formation of a polycrystalline layer on substrate during vapor condensation (island growth), that corresponds to Volmer-Weber growth mode. This mode is realized when reverse inequality $\gamma_s \leq \gamma_f+\gamma_{sf}$ is satisfied.

Formation of a single-crystal branch of the first order in an amorphous film and growth of the second order branches on their lateral surface (mode of DPC) correspond to Stranski-Krastanov growth mode (layer-plus-island growth). This mode is realized initially when $\gamma_s \geq \gamma_f+\gamma_{sf}$. Then, after critical thickness, when $\gamma_s \leq \gamma_f+\gamma_{sf}$.

REFERENCES

[1] V. Yu. Kolosov, A. R. Thölén, *Acta Mater.*, **48**, 1829 (2000).
[2] A. G. Bagmut, *Tech. Phys. Lett.*, **38**, 488 (2012).
[3] A. G. Bagmut, *J. Cryst. Growth*, **492**, 92 (2018).
[4] A. N. Kolmogorov, Izv. Akad. Nauk SSSR, Ser. Mat. **3**, 355 (1937).
[5] V. Z. Belen'kii, Geometric-Probabilistic Models of Crystallization: A Phenomenological Approach (Nauka, Moscow, 1980) [in Russian].
[6] A. G. Bagmut, *Phys. Solid State*, **59**, 1225 (2017).
[7] A. G. Bagmut, I.A. Bagmut, *Functional Materials*, **25**, 525 (2018).
[8] E. Bauer, H.Poppa, *Thin Solid Films*, **12**, 167 (1972).

NANOMATERIALS SCIENCE & ENGINEERING
Vol. 1, No. 1, pp. 34-41 (2019)

RESEARCH ARTICLE

https://proa.ua.pt/index.php/nmse/

Influence of Niobium additions on sintering behaviors and mechanical properties of injection molded 420 stainless steel powder

Lutfi Yakut [1], H.Ozkan Gulsoy [2] *

[1] Marmara University, Inst. Graduate Studies Pure and Applied Sci., 34722, Istanbul, Turkey
e-mail address: lutfu_yakut@hotmail.com
[2] Marmara University, Technology Faculty, Metallurgy and Materials Eng. Dep., 34722 Istanbul, Turkey
**Corresponding author, e-mail address: ogulsoy@marmara.edu.tr*

Received 16 October 2019; accepted 3 December 2019; published online 19 December 2019

ABSTRACT

This paper describes the sintering of an injection molded 420 martensitic stainless steel with additions of niobium, with the aim of producing high mechanical properties. And at the same time, microstructural and mechanical characterization of these produced parts was also carried out. At the initial stage, 420 martensitic stainless-steel powders were mixed with a multi-component binder system for preparing feedstock. Then the prepared feedstock was granulated and shaped by injection molding. And then, the shaped samples were subjected to the debinding process. These samples were sintered at different temperatures for various times. Samples sintered under the condition that gave way to the highest relative density were heat treated. Sintered and heat-treated samples were separately subjected to microstructural and mechanical characterization. All analysis showed that using polymeric binder system led to plentiful martensite ratio and carbide precipitates to be occurred in the injection molded samples. Mechanical characterization was performed by hardness measurements and tensile tests.

1. INTRODUCTION

Powder injection molding (PIM) is a powder metallurgy process currently used for the production of complicated and near-net-shape parts of high-performance materials. This technique basically combines the advantages of the plastic injection molding with the versatility of the traditional powder metallurgy, producing highly complex part of small size, tight tolerance, and low production cost. The process overcomes the shape limitation of traditional powder compaction, the cost of machining, the productivity limits of isostatic pressing and slip casting, and the defect and tolerance limitations of conventional casting [1-4]. Mechanical properties of a well-processed powder injection molded material and indistinguishable from cast and wrought material. The PIM process is composed of four sequential steps; mixing of the powder and organic binder, injection molding, debinding (binder removal), and sintering. If it is necessary, secondary operations such as heat and surface treatments after sintering can be performed [1-2].

AISI 420 stainless steel has high chromium (12 to 14%) and medium carbon content (> 0.15%) in its chemical composition [5]. Following heat treatment, the material has useful properties including high strength, hardness and corrosion resistance [6], making it a suitable choice for wear applications [7]. Although there are some experimental studies on PIM of 420 stainless steels, more detailed information is not available in literature. In particular, the effect of the niobium element on 420 stainless steels is unknown.

Previous works on PIM of 420 stainless steel less discussed mechanical properties and microstructure [8, 9].

Nb has a higher affinity for C than Cr. In low C alloy steels, the addition of Nb has been reported to improve the mechanical properties [8-10]. It was reported that, in presence of Nb, yield strength of high strength low alloy (HSLA) steel increased from 700 to 780 MPa. Nb can also reduce the hardenability of steel because it forms very stable carbides [11], thereby reducing the 4 amounts of C dissolved in the austenite during heat treatment. Another role of Nb in cast and wrought stainless steels is as a stabilizing agent to reduce the tendency to undergo intergranular corrosion. Though 420 stainless steel possessed good corrosion resistance in the heat-treated condition, which depletes the Cr content in solution near the grain boundaries and thus reduces the intergranular corrosion resistance significantly [12-15].

This present work was aimed to investigate the effect of Nb on the sintering behavior and the final properties of powder injection molded 420 stainless steel. Metallographic techniques were employed to sintered tensile bars to investigate the sintering behaviors. Tensile, hardness and corrosion properties of the sintered products were evaluated in heat-treated condition. Powder morphology, molded, debinded, sintered and heat-treated samples were analyzed under scanning electron microscope.

2. EXPERIMENTAL PROCEDURES

The powder chemical properties and characteristics of gas atomized 420 and 420+Nb stainless steel powders used in this study are given Table 1 and 2. Particle size distributions indicate similar median particle sizes for two type powders. Morphology of the powders, observed using scanning electron microscopy are given Fig. 1(a) and (b). All powders are spherical in shape.

Table 1. Chemical composition of 420 and 420+Nb stainless steel powders.

	Elements (wt.%)											
	Fe	Nb	Mo	Cr	Ni	Mn	Si	P	C	S	O	N
AISI Standart	Bal.	--	--	12-14	--	<1.0	<1.0	<0.04	>0.15	<0.03	--	--
420	Bal.	NA	NA	12.8	NA	0.72	0.79	0.012	0.3	0.01	0.04	0.09
420+Nb	Bal.	1.0	0.56	12.0	0.65	0.9	0.9	0	0.3	0	NA	NA

Table 2. Powder characteristics of 420 and 420+Nb stainless steel powders.

Item	420 SS	420SS + Nb
Vendor	Osprey Co.	Osprey Co.
Production method	Gas atomized, N	Gas atomized, N
Shape	Spherical	Spherical
Particle size (μm)		
D_{10}	4.30	5.07
D_{50}	12.55	11.78
D_{90}	26.64	21.80
Tap density, g/cm^3	4.70	4.90

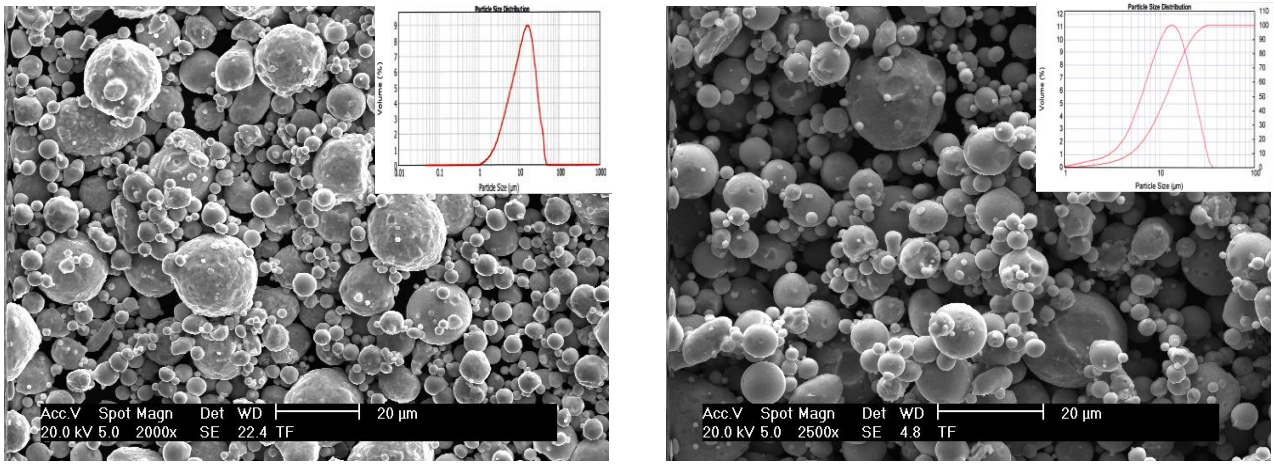

(a) (b)

Figure 1. Scanning electron micrograph of 420 and 420+Nb stainless steel powder (a) 420 and (b) 420+Nb.

Paraffin wax (PW), carnauba wax (CW), polypropylene (PP) and stearic acid (SA) were used as multi-component binder system to prepare the feedstocks. A multiple-component binder system consisting of PW (69 wt%), PP (10 wt%), CW (20 wt%) and SA (1 wt%) was employed. In order to observe the temperature on rheological behavior of feedstocks. Powder was prepared in formulations containing as 62.5 % vol. Feedstocks were prepared by means of blade mixer. Feedstocks for each volume of component were separately prepared at 180 °C throughout obtaining homogeneous mixing separately. Cooled feedstocks were granulated and then denominated for 62.5 % vol. Rheological behaviour of the feedstocks was measured using a rotational Rheometer Physica MCR51 (Anton Paar. Austria) at shear rates from 10 to 1.000 s-1 at temperatures 120-170°C. The value of viscosity is given by the shear stress divided by the shear rate.

After cooling, the feedstock was pelletized by hand. These feedstocks were injected using a 12.5 MPa specially made injection-molding machine to produce standard tensile test specimens. During which the melt temperature of 180 ºC, the mold temperature of 35 ºC and cycle time of 20 second were used to produce green tensile samples. Debinding was conducted in a two-step solvent/thermal operation. Green parts were solvent debound at 60 ºC for 4 h in hexane, followed by thermal debinding step at 1.8 ºC/min to 600 ºC for 1 h and pre-sintered at 4 ºC/min to 900 ºC for 1 h in pure Ar. The samples were sintered in an atmosphere controlled vertical recrystallized alumina tube furnace. The sintering cycle applied to the samples was as follows; samples were heated to 1200 ºC at a rate of 10 ºC/min and held at 1200 ºC for 5 min., then the samples were heated to various sintering temperatures of 1250 ºC, 1300 ºC and 1350 ºC at a rate 5 ºC/min and they were held at each temperature for 1 hour in Ar.

Densities of the sintered tensile bars were measured by the Archimedes method. The samples were cut from the tensile bars, mounted, ground, and polished to a 0.3 μm and 0.5 μm surface finishing using standard metallographic procedures. A Kalling's reagent was used to etch the samples for optical metallography. Finally, the sintered tensile bars were heat-treated the following two steps. The heat treatment consisted of a solution treatment in argon for 1 hour at 1030ºC, followed by an air quench and aging treatment for 1 hours at 440ºC with a cooled in air. All tensile tests were performed using Zwick-Z250 mechanical tester at constant crosshead speed of 25.4 mm/min (25 mm gauge length). The hardness tests were performed using an Instron-Wolpert Dia Testor 7551 at HRC scale. An average of five values of all mechanical measurements was reported. The fractures were examined using a scanning electron microscope (FEI-Srion).

2. RESULT and DISCUSSION

The evaluation of the feedstock rheological properties is based on the viscosity and its shear rate, temperature and powder type sensitivity. The lower the value of the viscosity, the easier it is for a feedstock to flow. It can be found from Fig. 2. that the viscosity decreases at all shear rates. With the increase of temperature, viscosity of feedstock decreases for two types powder. PIM feedstock is conducted under pressure and temperature. It is desirable that the viscosity of the feedstock should decrease quickly with increasing shear rate during molding. This high shear sensitivity is especially important in producing complex parts. In addition, the surfaces of the 420+Nb powders are smoother. Therefore, they are better connected with binders. As a natural consequence, the viscosity values were lower compare to 420 stainless steel powder. The results indicate that the feedstocks possess pseudo-plastic rheological behavior and increasing temperature leads to a decrease in the viscosity.

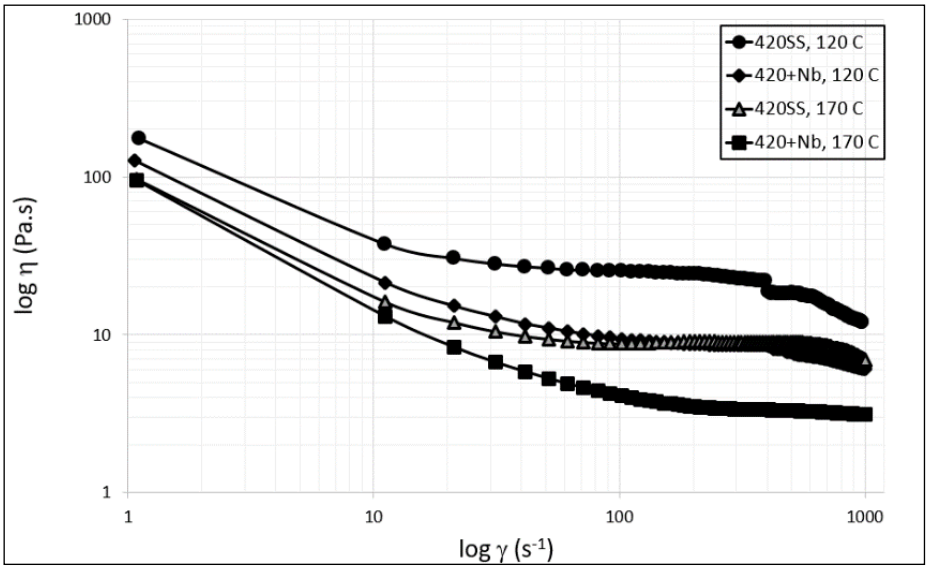

Figure 2. Temperature-dependent viscosity versus shear rate of different type 420 and 420+Nb stainless steel powder.

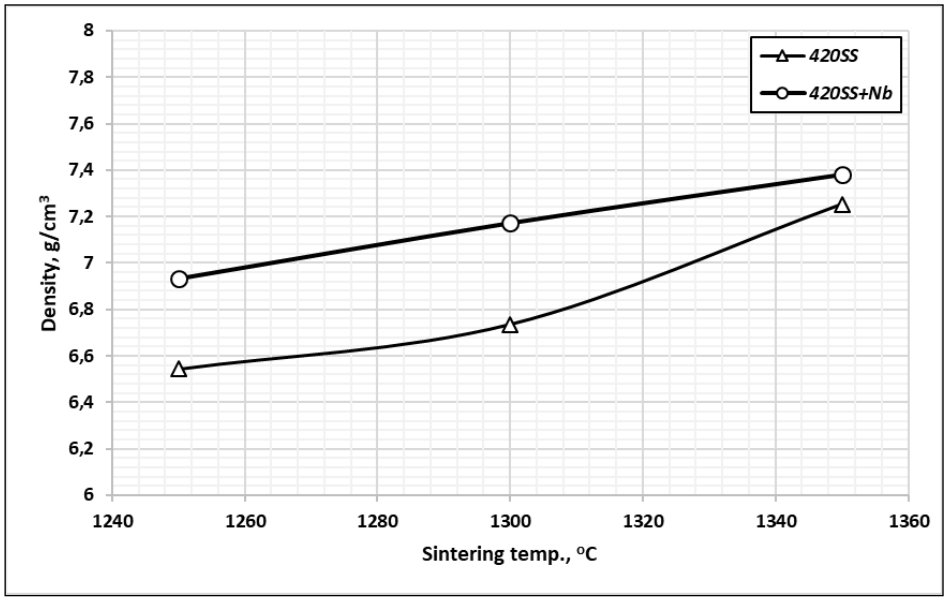

Figure 3. Sintered density of the samples sintered at different temperatures

Fig. 3 shows the change in sintered density values for two different types of 420 stainless steel powder depending on the increasing sintering temperature. In both types of powder, sintered densities of samples increased depending on the increasing sintering temperature. Compared to sintering densities at all sintering temperatures, 420 stainless steel samples showed lower density values than 420+Nb stainless steel samples. The sintered densities of the samples sintered were 6.54 g/cm^3 for 420 stainless steel samples and 6.93 g/cm^3 for 420+Nb stainless steel samples at 1250 ºC, respectively. With increasing sintering temperature, sintered densities reached to 7.25 g/cm^3 for 420 samples and 7.38 g/cm^3 for 420+Nb samples at 1350 ºC, respectively. In general, increased sintering temperature and Nb addition has improved sintering behavior.

Metallographic analysis was carried out on samples from each type samples for different sintering temperatures. Images of the polished microstructures for two types samples are shown in Fig. 4. At lower sintering temperatures, polished surfaces were present more pores. But at higher sintering temperatures, the pore quantity is low. This is a natural result of increased sintering temperature. At the same time, when Nb addition and non-added samples were compared, it was found that there was less pores in Nb added samples. Images of the etched samples microstructures for two types samples are shown in Fig. 5. The microstructure showed needle-liked structures that were dispersed throughout the etched microstructure representing a martensitic structure in the heat-treated conditions. The microstructures exhibited by the two materials types are quite different. The 420SS without Nb displays predominantly intergranular eutectic precipitation surrounding large grains with little intragranular carbide. The 420SS containing 1%Nb exhibits a much finer and uniform grain size with extensive intragranular precipitation of NbC. Finally, the Nb alloy-based samples shows residual porosity, intermediate grain size and a lower concentration of intragranular NbC precipitation reflecting its lower Nb content. Martensite forms through austenite-martensite transformation in the range from 700 to 300°C when the cooling is rapid.

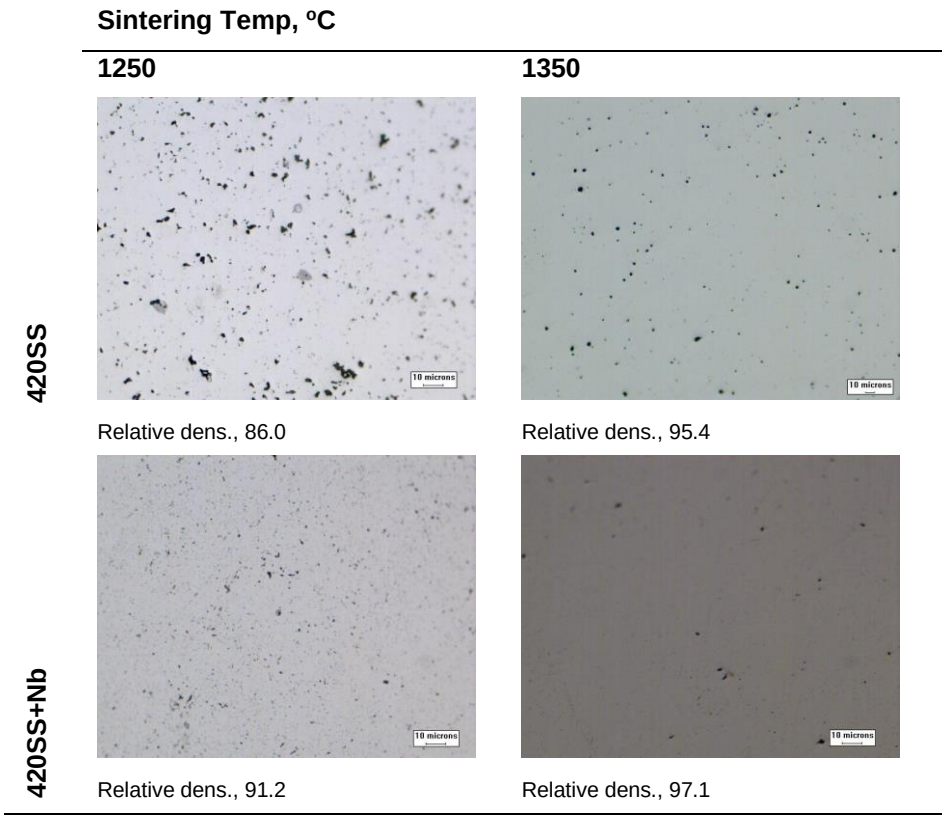

Figure 4. Microstructures of as-polished samples sintered at 1250 ºC and 1350 ºC for 1 h.

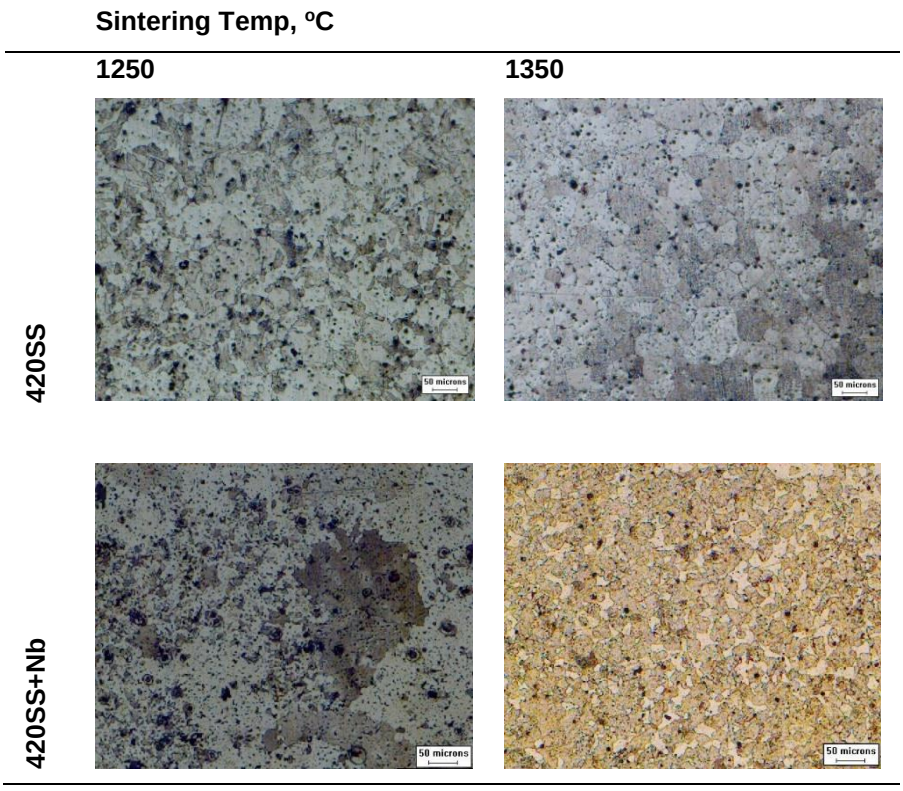

Figure 5. Microstructures of as-ethected samples sintered at 1250 ºC and 1350 ºC for 1 h.

Table 2. Mechanical properties of sintered and heat treated 420 and 420+Nb stainless steel samples

Sample (at 1350 °C-1 h.)	**Sintered density gr/cm^3**	**Ultimate tensile strength MPa**	**Yield strength MPa**	**Elongation %**	**Hardness HRC**
420 SS	7.25	901	817	1.6	47.2
420+Nb SS	7.38	1323	1152	2.9	49.3
420 (MPIF 35) [12]	7.40	1380	1200	<1	44.0

Microstructures of sintered samples shows tempered martensite in all cases with fine chromium and niobium carbides dispersed throughout the matrix. The carbides formed at the grain and grain boundaries caused an increase in mechanical properties.

The mechanical properties of the samples that were processed under different sintering temperatures are shown in Table 2. Graphs of comparison of mechanical properties results were shown in Fig. 6. The effect of Nb additions on the ultimate tensile strength, yield strength, elongation and hardness of 420 and 420+Nb stainless steels in sintering temperature at 1250-1350 ºC are shown in Fig. 6. Ultimate tensile strength, yield strength, elongation and hardness increase with Nb additions and sintering temperature. The maximum ultimate tensile strength of 1323 MPa, yield strength of 1152 MPa, elongation of 2.9 and hardness of 49.3 HRC was reached with samples added Nb sintered at 1350 ºC for 1 h. Depending on the increase in sintering temperature, grain size increased. At the same time, chromium and niobium carbides were formed at high sintering temperatures. Due to grain size increase and carbide formation, mainly sintered densities and mechanical properties increased.

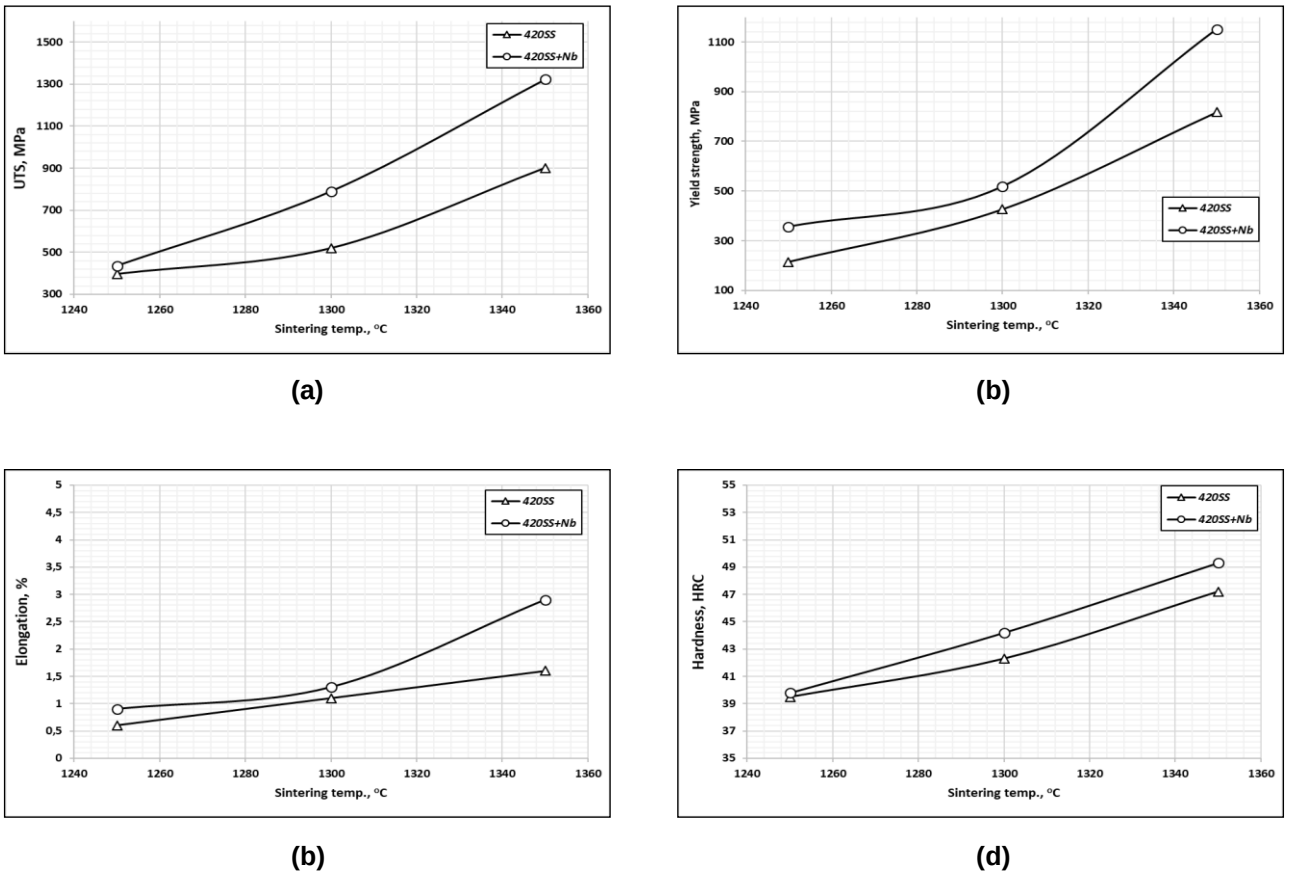

Figure 6. Effect of sintering temperature and Nb addition of mechanical properties of 420 stainless steel. (a) Ultimate tensile strength, (b) Yield strength, (c) Elongation, (d) Hardness.

More importantly, the formation of martensite phase is the main reason for the increase in mechanical properties. The mechanical properties of the Nb added samples exhibited higher values when compared with the addition and addition of Nb.

3. CONCULUSION

This study concluded that the pre-alloying of 1 wt.% Nb significantly affected the properties and microstructure powder injection molded 420 stainless steel in the sintered and heat-treated conditions. In conclusion, experimental results show that the 420 and 420+Nb stainless steels materials can be produced using PIM techniques. The addition of Nb elements provided some benefit in terms of densification, strength, elongation and hardness. The maximum sintered density achieved in this investigation was 7.38 g/cm3 for a 420+Nb materials. Tensile strength of 1323 MPa, elongation of 2.9% and hardness of 49.3 HRC were achieved for 420+Nb addition. The conditions used for processing these materials lead to good conformity, allowing the improvement of some mechanical properties.

Acknowledgements

The authors are grateful to Marmara University (Project No.: FEN-C-YLP-121218-0618) and Sandvik Osprey Ltd. for their financial support and the provision of laboratory facilities.

REFERENCES

[1] R. M. German and A. Bose: 'Injection molding of metals and ceramics', 17–25, (1997), New Jersey, MPIF.
[2] R. M. German: 'Powder injection molding', 7–10, (1990), New Jersey, MPIF.
[3] H.O. Gulsoy, *Mater. Sci. Technol.* **24 (12),** 1484–1491 (2008).
[4] H.O. Gulsoy, S. Ozbek, T. Baykara, *Powder Metall.* **50 (2),** 120–126 (2007).

[5] A.J Coleman, K. Murray, M. Kearns, T.A. Tingskog, B. Sanford, E. Gonzalez, http://www.materials.sandvik/ (2019)
[6] D. Li, H. Hou, L. Liang, K. Lee, *Int. J. Adv. Manuf. Technol.* **49**:105–110 (2010).
[7] Y. Shan, X. Luo, X. Hu, S. Liu, *Journal of Materials Science & Technology*, **27**, 352-358 (2011).
[8] M. Hua, C. Garcia, A. DeArdo, *Metall. and Mater. Trans. A*, **28**, 1769-1780 (1997).
[9] N. Fujita, K. Ohmura, A. Yamamoto, *Materials Sci. and Eng. A,* **351**, 272-281 (2003).
[10] K. Taylor, *Scripta Metall.* **32**, 7-12 (1995).
[11] C. Rodrigues, P. Lorenzo, A. Sokolowski, C. Barbosa, J. Rollo, *Mater. Sci. and Eng. A.,* **460**, 149-152 (2007).
[12] Standard, M., 35–Materials standards for structural parts. Metal Powder Industries Federation, 2016, 32-35.
[13] F.R.A. Jeglitsch, *International Symposium on Niobium*, 1001-1039 (2001).
[14] A.J. DeArdo, *International Materials Reviews,* **48**,.371-402 (2003).
[15] M.A. Kearns, M.K. Johnston, K. Murray, P.A Davies, V. Ryabinin, E. Gonzalez, *Int. J. Powder Metallurgy,* **52**, 15-24 (2016).

NANOMATERIALS SCIENCE & ENGINEERING
Vol. 1, No. 1, pp. 42-49 (2019)

RESEARCH ARTICLE

https://proa.ua.pt/index.php/nmse/

Study the influence of the pre-finish gauges form on the effectiveness of the grooves filling in the finishing pass of reinforcing steel rolling

Olesya Fedchenko[1*], Olga Krivtsova[1], Evgeniy Panin[1*], Sergey Lezhnev[2]

[1] Karaganda state industrial university, 101400, Republic avenue 30, Temirtau, Kazakhstan,
**Corresponding author, e-mail address: fedchenko.kadzhu@mail.ru*
[2] Rudny industrial institute, 111500, 50 let Oktyabrya 38, Rudny, Kazakhstan,
**Corresponding author, e-mail address: sergey_legnev@mail.ru*

Received 16 October 2019; accepted 5 December 2019; published online 19 December 2019

ABSTRACT

During reinforcing steel rolling such geometric defect as the absence of longitudinal or transverse ribs is spread. For a detailed study of the process of reinforcement profile rolling and its further optimization, computer simulation in the software complex DEFORM-3D was carried out. In the previous works the most rational, from the authors' point of view, forms of pre - finishing gauges for rolling of reinforcing steel are proposed - a one-radius oval and a flat oval with double concavity. Also, a new calibration for rolling of round and reinforcing steel was proposed, the main feature of which is the pre-finishing caliber, made in the form of a smooth barrel. To assess the impact of the pre-form gauge on the strain state, a single simulation was conducted, i.e. modeling only the pre-finishing caliber, after which the calculation of the finishing pass was conducted.

From considered calibers, the most uniform distribution of deformation provides a flat oval with double concavity, where the distribution in the vertical and horizontal directions is approximately the same. In other two calibers, the spread difference is quite different. After rolling in the finishing pass, the metal completely filled the contour of the caliber, as well as the screw incisions of the transverse ribs. The longitudinal ribs are also fully formed. All geometric parameters with tolerances fully comply with the requirements of GOST 10884-94.

1. INTRODUCTION

Reinforcing steel is used for the manufacture of reinforcement of concrete structures. Reinforcing steel in concrete structures is installed mainly for the perception of tensile forces and strengthening of concrete compressed zones of structures. The strength characteristics of the reinforcing steel depend on the chemical composition of the steel (carbon content, alloying additives) and the nature of its processing (cold hardening of steel by drawing, drawing, flattening, heat treatment, etc.). Despite the constant improvement of the rolling technology in the production of rolled steel products is still a high proportion of the yield of metal in marriage. In particular, during reinforcing steel rolling, such a geometric defect as the absence of longitudinal or transverse ribs is common. It is known [1, 2] that for the best filling of finishing gauges of any shape it is necessary not only to ensure its exact execution of geometric dimensions, but also, if possible, to minimize the anisotropy of mechanical properties throughout the

cross section of the deformable metal. If in the first case it is necessary only to comply with the requirements of GOST on the geometric dimensions of the caliber, taking into account the temperature expansion of the metal, then the second task has some difficulties, since it is quite difficult to predict the distribution of the accumulated deformation for all passes as a whole, and for individual calibers. In particular, of great interest is the shape and size of the finishing gauge, after which the roll falls into the finishing gauge, where the final profile is formed. In this work the simulation results of rolling in pre-finish gauges of various form and distribution of strain and rolling forces are presented.

2. PREPARATION OF MODEL

For a detailed study of the process of rolling the reinforcement profile, it was decided to conduct computer simulation in the software complex "Deform-3d". The paper proposes the most rational, from the point of view of the authors, forms of finishing gauges for rolling reinforcing steel. However, there is a controversial question about the so-called "transition" profiles, which some authors refer to small profiles, and others – to large; in particular, profile number 20. For this profile, both an one-radius oval and a flat oval with double concavity are offered as a finishing gauge [3]. Also, in the works [4-5] a new calibration for rolling round and reinforcing steel was proposed, the main feature of which is the pre-finishing caliber, made in the form of a smooth barrel. Therefore, to determine the most rational form of the pre-finishing caliber, it was decided to simulate rolling in all three calibers in order to identify the most uniform distribution of the accumulated deformation across the cross section of the workpiece.

Since deformation is a cumulative parameter, it is very difficult to track its change at any particular stage in the analysis of the entire technological process. Therefore, in order to assess the effect of the shape of the pre-finishing caliber on the deformed state, a single simulation was carried out, i.e. the model included only the pre-finishing

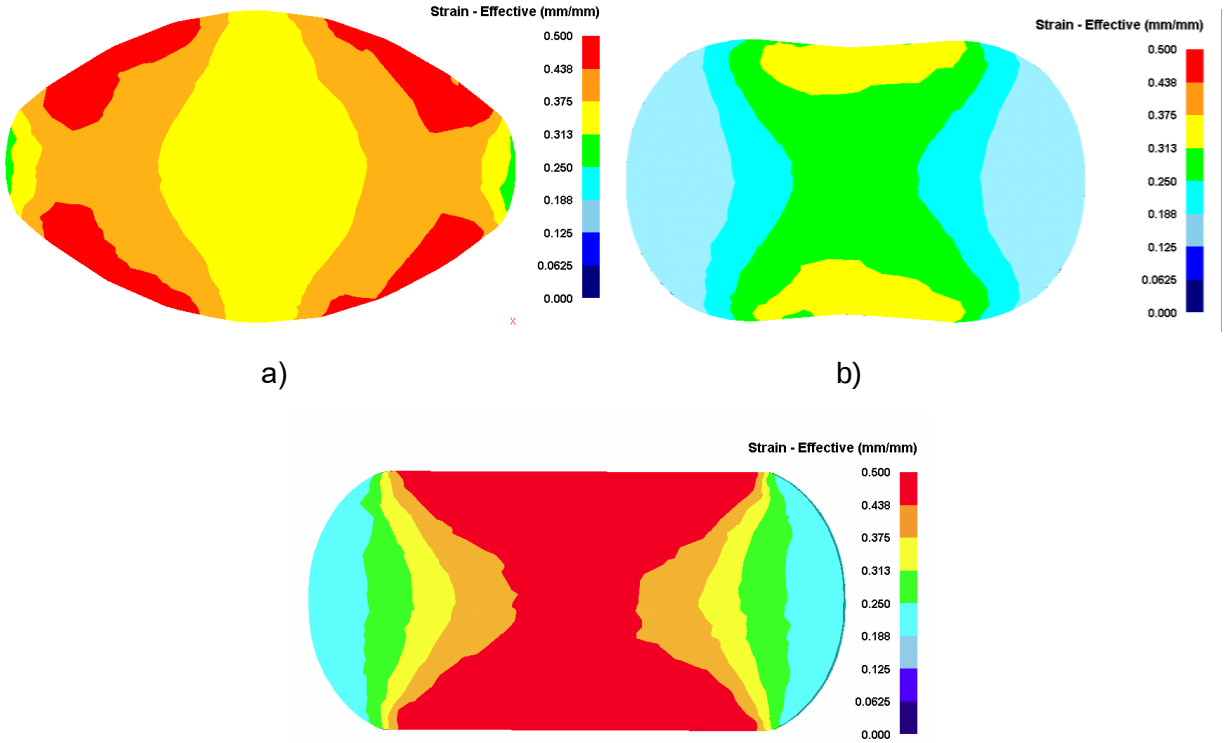

Figure 1. Distribution of equivalent strain. a) one-radius oval; b) flat oval with double concavity; c) smooth barrel.

caliber. In all 3 cases the workpiece was elastic-plastic type. The steel AISI 1035 was chosen as material. The initial workpiece temperature was 900 °C. The friction coefficient on the contact of workpiece and rolls was 0.3. The angular velocity of rolls was 90 rpm, radius of rolls was 320 mm. The initial billet had round cross-section with a diameter 25 mm and length 200 mm.

As a result of modeling the following distribution patterns of equivalent strain were obtained (Figure 1).

For a detailed study of the distribution of equivalent strain on the cross section, two directions were considered: vertical and horizontal, since before entering the final gauge, the workpiece in all three cases is subjected to a 90 degree turning. The rolling force generated by the deformation in these gauges was also considered in order to estimate how much the force value changes compared to the reference value. For the reference force value was adopted value received in one-radius oval, as the caliber is most common for section mills, rolled reinforcing profiles.

3. RESULTS AND DISCUSSION

3.1. One-radius oval

When rolling in a caliber in the form of a one-radius oval, the distribution of deformation is extremely uneven. With a fairly uniform distribution in the axial zone (Figure 2), when moving to the walls of the caliber, the deformation values increase sharply, especially on inclined sections of the roll. At the same time, on the side ends, on which the formation of transverse ribs occurs after the edging, there is a significant decrease in the deformation value (Figure 3).

1

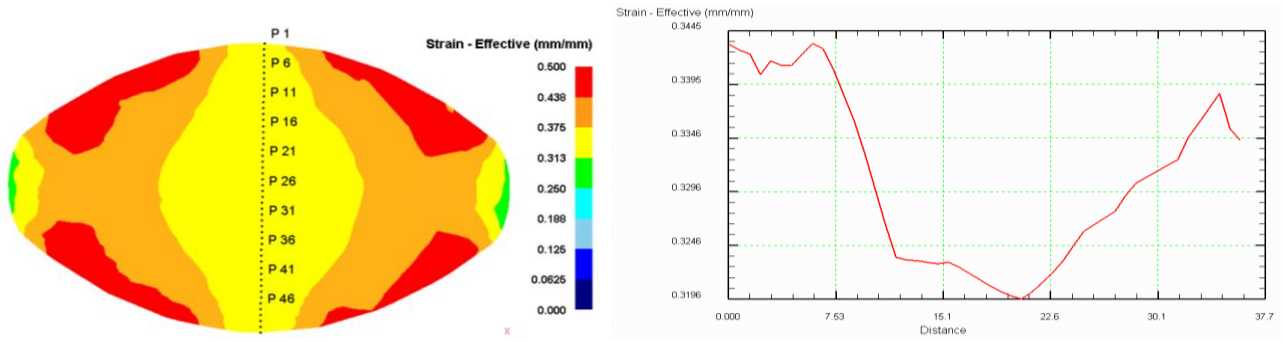

Figure 2. Distribution of deformation during rolling in a one-radius oval in the vertical direction.

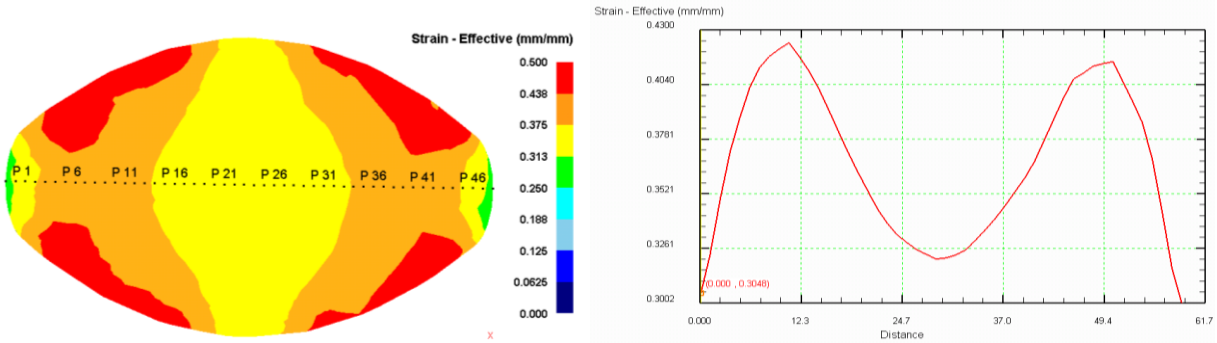

Figure 3. Distribution of deformation during rolling in a one-radius oval in the horizontal direction.

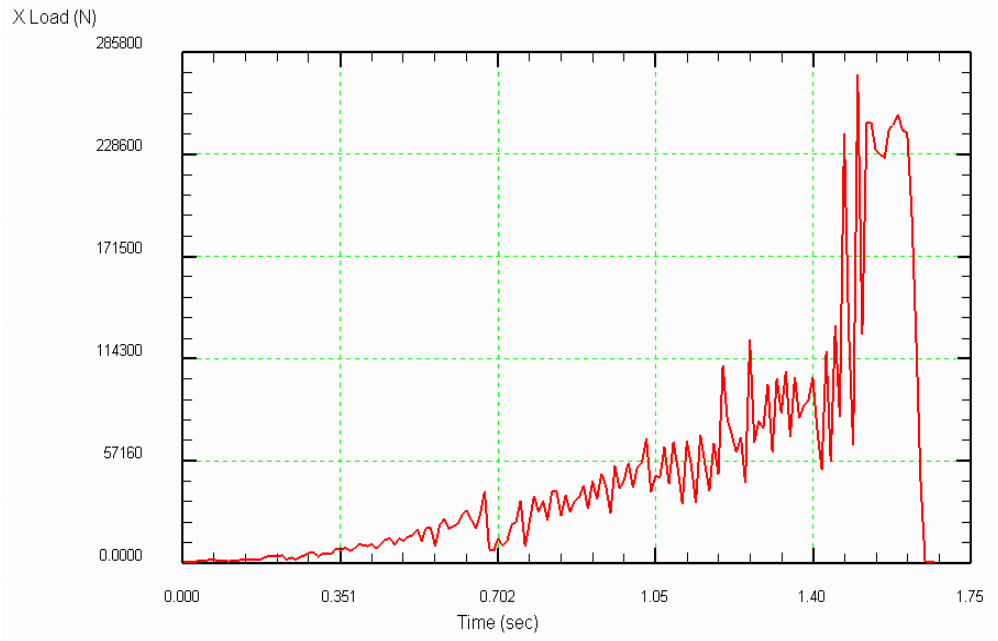

Figure 4. Rolling force in an one-radius oval.

In the vertical direction, the strain distribution is from 0.3195 to 0.3435 (value spread = 7.5 %). In the horizontal direction, the strain distribution is from 0.3008 to 0.4248 (value spread = 41.2 %). When taking into account the inclined zones, where the deformation value reaches a value of 0.5, the spread is 66.2 %.

Two zones are clearly visible on the force graph: in the first zone, characterizing the capture of the workpiece, the force increases smoothly as the deformation center is filled. With the steady-state rolling process, the force value remains at the same level and is approximately 251.5 kN (Figure 4).

During rolling in a caliber in the form of a flat oval with double concavity, the distribution of deformation in the vertical and horizontal directions proceeds more evenly compared to a one-radius oval. In the axial zone, there is some increase in deformation due to concavities (Figure 5). At the lateral ends, the distribution of the deformation value is more uniform than in a one-radius oval (Figure 6). This is confirmed by the strain distribution graphs – in the first case, the peaks characterizing the sharp increase are clearly visible, then the decrease and then the increase in the strain value. In the second case, the graph is more monotonous.

3.2. Flat oval with double concavity

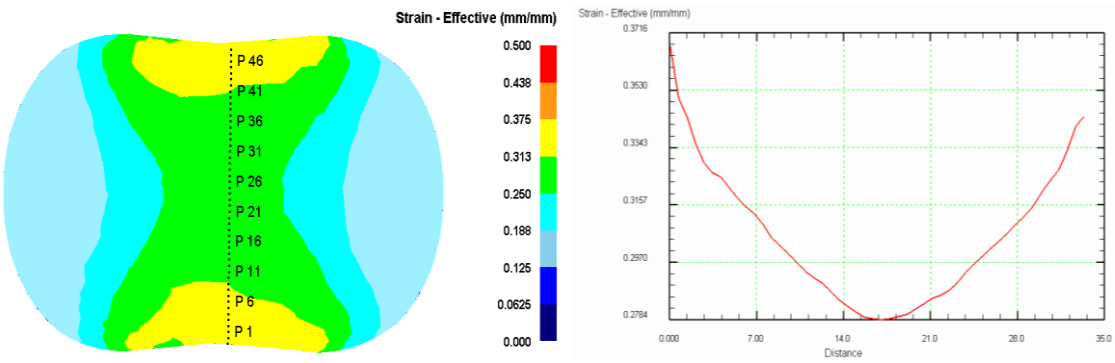

Figure 5. Distribution of deformation during rolling in a flat oval in the vertical direction.

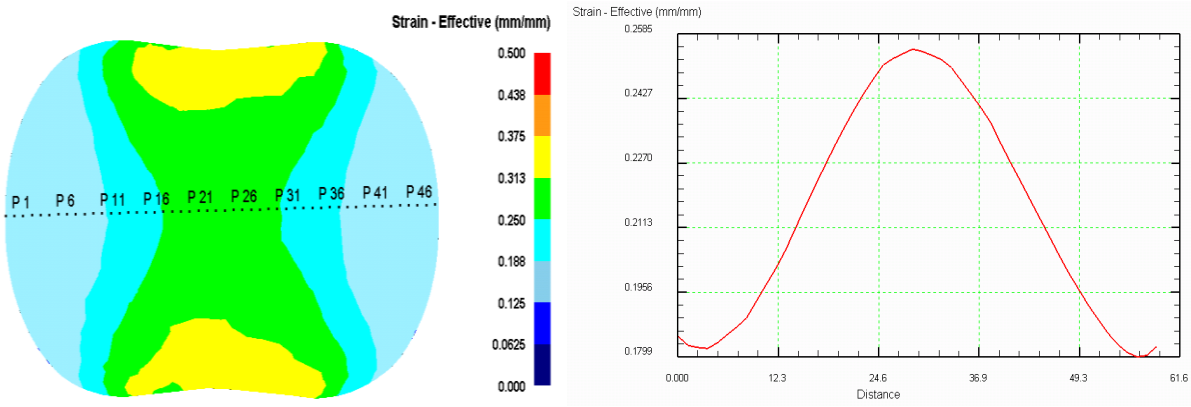

Figure 6. Distribution of deformation during rolling in a flat oval in a horizontal direction.

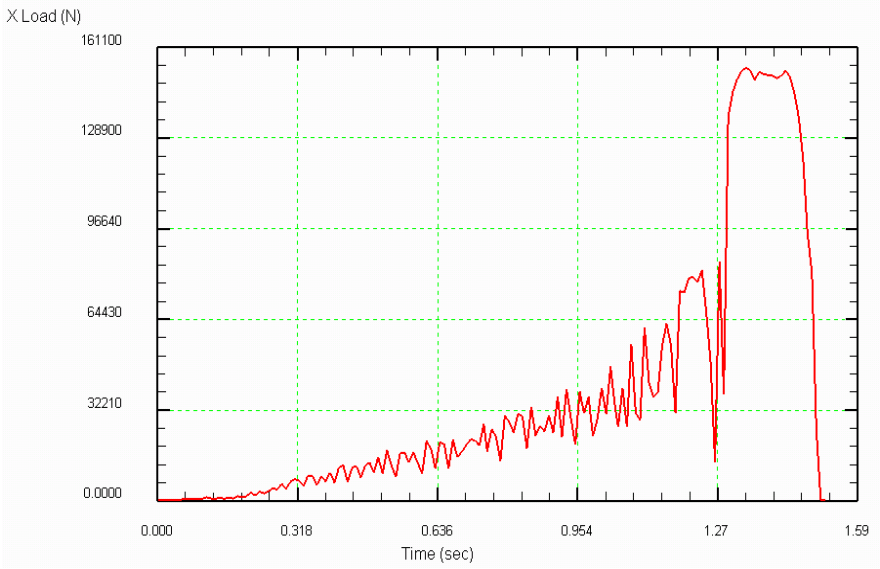

Figure 7. Rolling force in a flat oval with double concavity.

In the vertical direction, the strain distribution is from 0.2784 to 0.3678 (value spread = 32.2 %). In the horizontal direction, the strain distribution is 0.1799 to 0.2512 (value spread = 39.6 %).

The force graph, as in the first case, clearly shows two zones: the capture zone of the workpiece and the zone of the steady-state rolling process, where the force value remains at the same level and is approximately 154.6 kN (Figure 7).

3.3. Smooth barrel

When rolling on a smooth barrel, the distribution of deformation in the vertical and horizontal directions is very uneven. With a fairly uniform distribution in the axial zone (Figure 8), when moving to the side ends, where the metal contact with the rolls is absent, there is a significant decrease in the deformation value (Figure 9).

In the vertical direction, the strain distribution is from 0.4463 to 0.4705 (value spread = 5.4 %). In the horizontal direction, the strain distribution is from 0.2249 to 0.4517 (value spread = 100.8 %).

On the graph of effort, as in the above calibers, two zones are visible. In the area of the steady-state rolling process, the force value is approximately 184.3 kN (Figure 10).

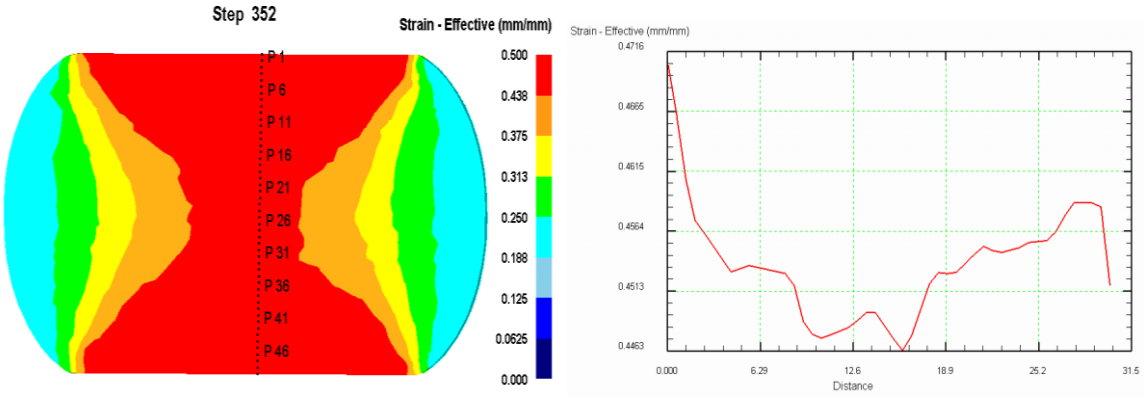

Figure 8. Distribution of deformation during rolling on a smooth barrel in the vertical direction.

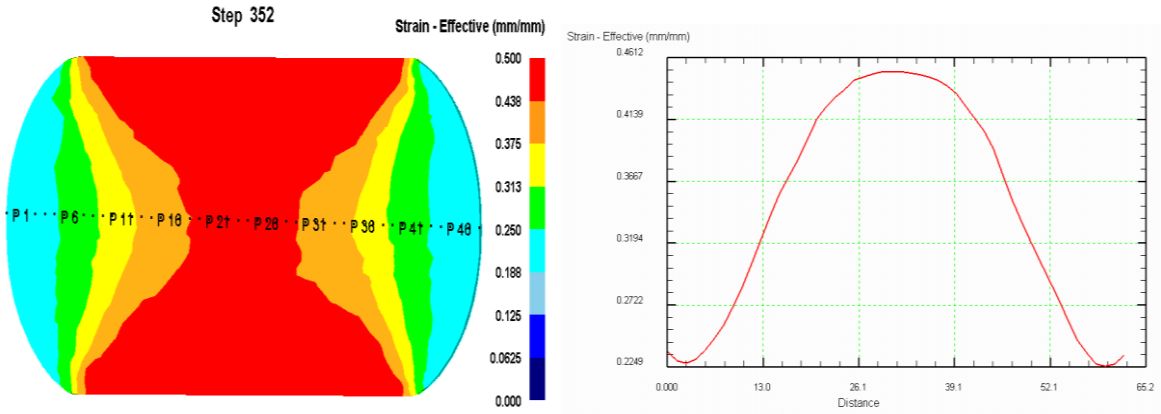

Figure 9. Distribution of deformation during rolling on a smooth barrel in the horizontal direction.

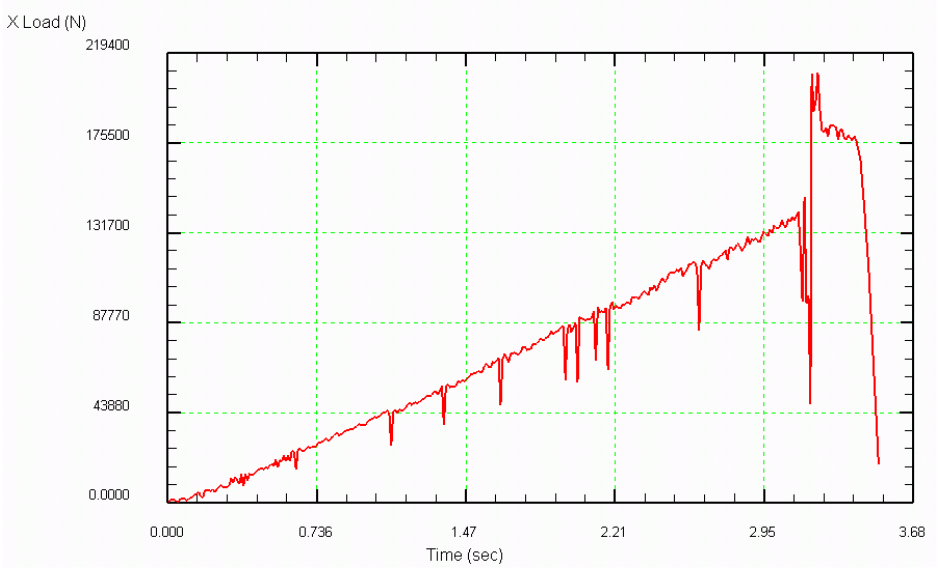

Figure 10. Rolling force on a smooth barrel.

When rolling in all three versions of the gauges, the distribution of deformation is uneven in the vertical and horizontal directions. Analysis of the force graphs showed that when rolling in a flat oval and on a smooth barrel, the force values do not exceed the value for a single-radius oval, which indicates the possibility of using these gauges on existing equipment without its modernization. From all considered calibers, the most uniform distribution of deformation provides a flat oval with double concavity, in which the spread in the vertical and horizontal directions is approximately the same; in the other two calibers, the difference in the dispersion is quite significant. As a result of the calculation of the model of the final caliber after rolling in a flat oval with double concavity, the following results were obtained (Figures 11-12).

After rolling in the finishing stand, the metal completely filled the contour of the caliber, as well as the screw cuts of the transverse ribs. Longitudinal ribs are also fully formed. The main requirements for geometric dimensions, according to GOST, are the correspondence of vertical and horizontal diameters d_1 and d_2, which characterize the height of the longitudinal and transverse ribs. The ovality of the section (the difference between d_1 and d_2 in one section) should not exceed the sum of the plus and minus limit deviations in size d1. In addition, an important characteristic of the geometry of reinforcing steel is the value t, which determines the distance between two adjacent transverse edges.

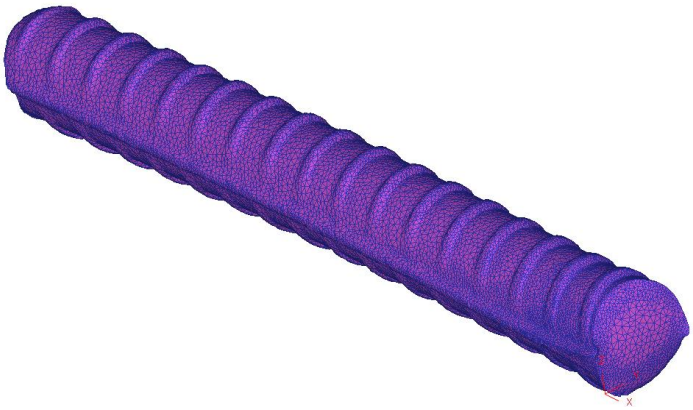

Figure 11. General view of the deformed workpiece.

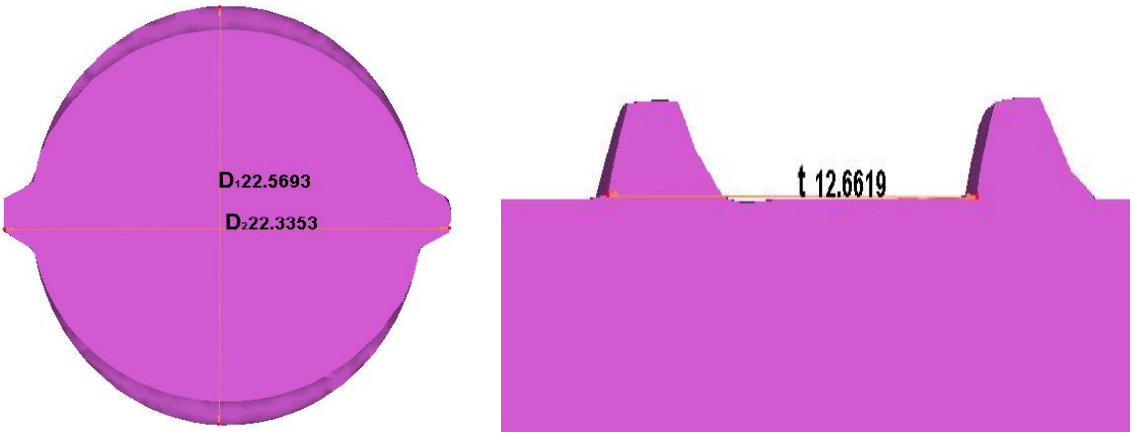

Figure 12. Cross and longitudinal section of the workpiece.

As shown in Figure 12, the value of d_1 in the resulting model is 22.569 mm, the value of d_2 is 22.335 mm. Deviation of d_1 is 0.269 mm, d_2 is 0.035 mm, which fully corresponds to the specified values of the limit deviations. The oval shape of the rod is 0.234 mm, which also meets the requirements of GOST. The value of t is 12.66 mm, which fully corresponds to the table value with a permissible limit deviation of ±15%, (in our case it is 5%).

4. CONCLUSION

1) After rolling in all 3 versions of calibers the strain distribution is uneven in vertical and horizontal directions;

2) The most even distribution of deformation provides flat oval with double concavity in which dispersion of the values in vertical and horizontal directions is approximately the same; in the other two calibers the difference of the dispersions are quite significant;

3) Analysis of the load graphs had showed that values of load at rolling in a flat oval and on the smooth barrel don't exceed a value for one-radius oval that says about the possibility of using these calibers on existing equipment without its modernization.

4) The model of the final caliber (reinforced profile) after rolling in a flat oval with double concavity showed, that obtained billet fully corresponds to the specified values of the limit deviations (two horizontal diameters and distance between two adjacent transverse edges).

REFERENCES

[1] V.K. Smirnov, V.A. Shilov, Y.V. Inatovich, *Calibration of rolling rolls, p. 138,* Teplotechnik, Moscow (2010).
[2] E.A. Ponle, O.B. Olatunde, O.W. Awotunde, Mechanical Properties of Reinforcing Steel Rods Produced From Recycled Scraps. *The International Journal Of Engineering And Science*. **3(2)**, 14-34 (2014).
[3] M.A. Benyakovsky, K.N. Bogoyavlensky, A.I. Vitkin, *Rolling production technology*. Metallurgy, Moscow (1991).
[4] V.N. Asanov, A.B. Steblov, O.N. Tulupov, Improvement of calibrations of rolls for rolling round and reinforcing profiles. *Steel*, **11**, 90-92 (2008).
[5] A.B. Steblov, V.N. Asanov, S.N. Berezov, Calibration for micro-plant for the production of construction fittings, *Calibration Bureau*, **1**, 43-46 (2013).

NANOMATERIALS SCIENCE & ENGINEERING
Vol. 1, No. 1, pp. 50-58 (2019)

RESEARCH ARTICLE

https://proa.ua.pt/index.php/nmse/

Comparison between linear and nonlinear tolerance analysis of flexible assembly taking into account spot welding effects

Boutahari Said*, Atik Hafsa, Chahbouni Mouhssine and Amegouz Driss

High School of Technology of Fez, University sidi mohamed ben abdellah B.P 2626 –Route d'Imouzzar, 30000 Fez, Morocco. mechanical engineering
**Corresponding author, e-mail addresses: said.boutahari@usmba.ac.ma, hafsa.atik@usmba.ac.ma, mouhssine.chahbouni@usmba.ac.ma, driss.amegouz@usmba.ac.ma*

Received 16 October 2019; accepted 5 December 2019; published online 19 December 2019

ABSTRACT

The tolerance analysis for flexible parts and assemblies is the precious step in manufacturing parts in industry. In order to minimize the cost of the process, the literature has focused on reviewing tolerance analysis for flexible parts and assemblies. In this paper, are developed two major methods of tolerance analysis for flexible assemblies. Furthermore, to improve the performance of the proposed model that has been simulated to predict the deformation of flexible parts and assemblies, we have taken into account the spot-welding effects. Finally, through a comparative study, the results prove the performances of the proposed approach.

1. INTRODUCTION

The technological choices were naturally oriented towards the use of flexible parts and assemblies because of the competition between industry for Sustainable development, energy saving, carbon footprint. The latter therefore offer flexibility for some directions of solicitation, which generates defects which can be categorized as follows two principal defects position, orientation or form. They are mainly derived from manufacturing processes, and accumulate during the assembly progresses.

Liu and Hu [1, 2] proposed methods of tolerance analysis of for non-rigid sheet metal assembly, this method is based on linear elastic mechanics relation between part deviation and to analyze the effect deformation and spring-back of the assembly by the construction of a sensitivity matrix to establishes the linear relationship between the part variation and the output assembly variation. This approach called Method of Influence Coefficients (MIC). Alain Stricher, in his paper [3], proposes to perform tolerance analysis on compliant structure by limiting the shape defects and connection defects in accordance to mechanical criteria with the method (MIC). As well as in his thesis [4] the objective is to enrich the method by taking into account the deformations of the parts involved by their assembly and their geometrical defects and the development of assembly assistance software. Due to the positioning errors of the plates, the defects geometry of the assembled structure can be caused whatever the assembly method used it the idea presented by Camelio and al [5].

To optimize the tolerance of the flexible parts and assemblies, [6, 7] introduce in the first step the factors influence the final quality of the assemblies. The first paper has for objective to study the model of simulation of the variation of flexible mechanisms, using the Influence Coefficient Method taking into account the effects of contact between the surfaces and including welding

distortion. In the second paper, we propose a new approach which takes into account shape defects based on the Influence Coefficient Method. Two models have been proposed to express tolerances and conduct tolerance analysis that gives more precise results; these methods are qualified as local and global methods [8]. The local method is based on the iterative calculation of mesh regularization. The global method is based on finite element analysis, with manufacturing deviations added to the nominal model by the penalty function approach. For the same aim of tolerance optimizing, the previous paper presents a new model to consider the form defects in an assembly simulation. A Metric Modal Decomposition (MMD) method is henceforth, developed to model the form defects of various parts in a mechanism. To achieve the automatic assembly of large-scale thin-walled structures, in [9] we propose to calculate the sizing force of the structures with deviations, and to study its assembling ability before assembly process, to establish a precise model to describe the deviations of structures and to study the variation propagation during assembly process. In the work [10], the objective was to present the influence of form deviations on the tolerance analysis of an assembly. For this they study initially the tolerance analysis using the deviations and clearances domains method, and in second time they integrate the influence of form tolerances on the allowable deviation domain.

2. THE NONLINEAR ANALYSIS METHOD OF FLEXIBLE ASSEMBLIES

To simulation sheet metal assemblies process it is very common, in various articles, to use Direct Monte Carlo Simulation with the introduction of the concept: cycle "CPRF" (Square Clamp Fasten and Release). The target is to predict the assembly variation based on parts variation. The snag is how much the variation of the assembly will be influenced by the parts variations (Figure1).

The behaviour of a part is expressed when the parts are loaded onto the work holding fixture. At that time the parts variations are recorded in vector $\{V_u\}$. Then the parts are forced to reach them nominal position, the first implementation of Finite element Method (FEM) is to calculate the forces applied to make the parts in them nominal position $\{F_u\}$ using the equation (1).

$[K_u]$ is the stiffness matrix of the structures.

$$\{F_u\} = [K_u]\{V_u\} \quad (1)$$

After that the parts are joined. The stiffness matrix raise from the matrix of the parts $[\mathrm{K_u}]$ to the matrix of the assembly $[\mathrm{K_w}]$. After we release of the assembled structure, the assembly will undergo spring-back from its nominal position.

$$\left\{ \begin{array}{l} [K_w]\{U_w\} = \{F_w\} \\ \{U_w\} = [K_w]^{-1}\{F_w\} \end{array} \right\} \quad (2)$$

Where $\{U_w\}$ is the spring-back of the assembly structures and $\{F_w\}$ is the force vector.

$\{\mathrm{F_w}\} = \{\mathrm{F_u}\}$ which connected between the spring-back $\{U_w\}$ of the assembled structure and the part deviations $\{V_u\}$ of the unassembled structure.

Figure 1. Nonlinear analysis method of flexible assemblies.

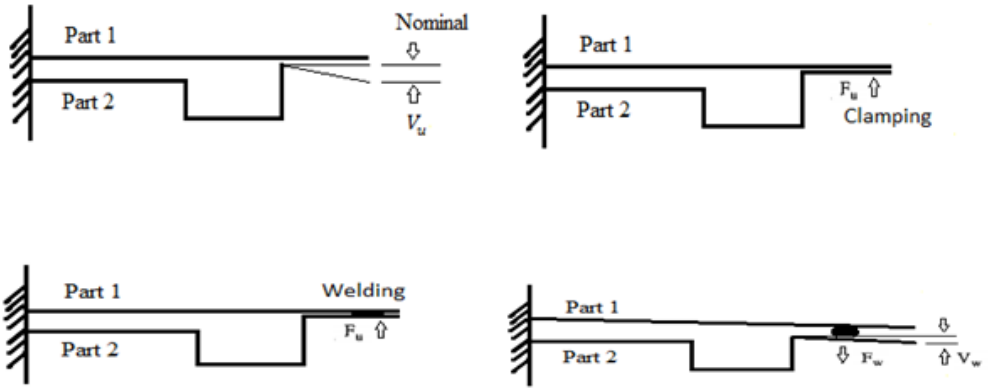

Figure 2. Cycle "CPRF" (Square Clamp Fasten and Release).

3. THE LINEAR ANALYSIS METHOD OF FLEXIBLE ASSEMBLIES

The principle of the Influence Coefficient Method is to establish a linear model between part deviations and assembly springback deviations, and that's why it is a way of performing the simulation faster than direct Monte Carlo. This method consists of three steps:

1. Force response on the displacements:

A unit force is applied to the j-th source of variation (j=1 to N) on the part. The source of variation could be any type of variation that the part will be subjected to. The response under that unit force the deformation of the part is calculated by Finite Element Analysis (FEA), and the displacements (i =1 to M) of the parts are recorded into a column vector Cj. We consider that the system is applied by an arbitrary combination of N forces (Fj, j=1 to N). [C] Is the matrix of Influence Coefficients and the vector {V} represents the deviations at the sources of variation.

$$\{\mathrm{V}\} = [\mathrm{C}]\{\mathrm{F}\} \quad (3)$$

2. Force response on the fixture points:

In step one, when a unit force is applied to the j-th source of variation, the reaction forces of the fixture points are recorded into a column vector Dj. The reaction forces R are the forces released during the springback process and [f] is the applied forces.

$$\{R\} = [D]\{f\} \quad (4)$$

3. Springback calculation of the assembly:

The springback displacements for the assembly are calculated with FEA similarly to step 1. The displacements of the points of interest are recorded into a column vector ***Sj*** for the assembly or the join parts. Here, the forces F are applied only to the

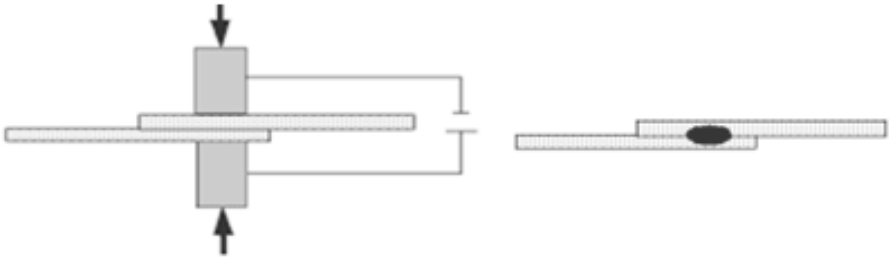

Figure 3. Two parts before and after they are joined together

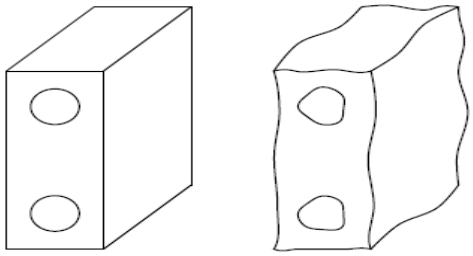

Figure 4. Skin-model concept.

fixture points or clamps that are released when the joining is done. Linear models between the applied forces F on the released fixture points and the springback displacements on final assembly could be derived by combining all the vectors ***Sj*** into a matrix:

$$\{U\} = [S]\{V\} \quad (5)$$

4. SPOT WELDING

A spot welding is modeled by a connection that passes through a point and connects two surfaces. Welds connect two or more thin overlapping metal sheets at small areas without using any filling material. Practical considerations set the limit on the total thickness of the joined sheets. The sheets are joined by applying local pressure and heat using shaped copper alloy electrodes. The electrodes apply adequate energy to cause the materials of the sheets to melt and mix together. After removing the electrodes, the melted material solidifies forming a nugget as shown in the Figure 3.

5. SKIN-MODEL CONCEPT

The "skin" model (Figure 4) that represents the interface of the part with its environment, with its defects. It differs from the nominal model that considers the parts with a perfect geometry.

6. PROPOSED METHODS

It is well known that there are many even contacts during the assembly process, such as contact between sample surfaces, contact between surfaces with fastening constraints, and the effect of tools (such as pistols welding). These paired contacts form the contact that propagate afterwards, and that caused the accumulating and stack dimensional variations. For the assembly of non-rigid parts, the deformation of the assembly makes the dimensional modeling more complex because of the propagation of variation of the parts, variations of the tool, and the deformation of contact after assembly.

In this part, the joining surfaces are supposed to be welded. Based on the flexible two-piece modeling assembly process, a new method for analyzing nonlinear contact modeling variation is proposed. Components are loaded and placed on fixed devices subsequently welded and release in the last phase according to the cycle "CPRF".

The procedure for performing a FEA, contact analysis is described by the steps shown in the following figure. As a result of the changes made for the improvement of the step method to create, the initial deformation the contact pattern is to identify where the contact could occur. For non-rigid assembly, the joint areas must be in contact. However, it is necessary to check if other areas are contacted during the assembly process. The targeted contact surfaces are defined for each pair of contacts are generated.

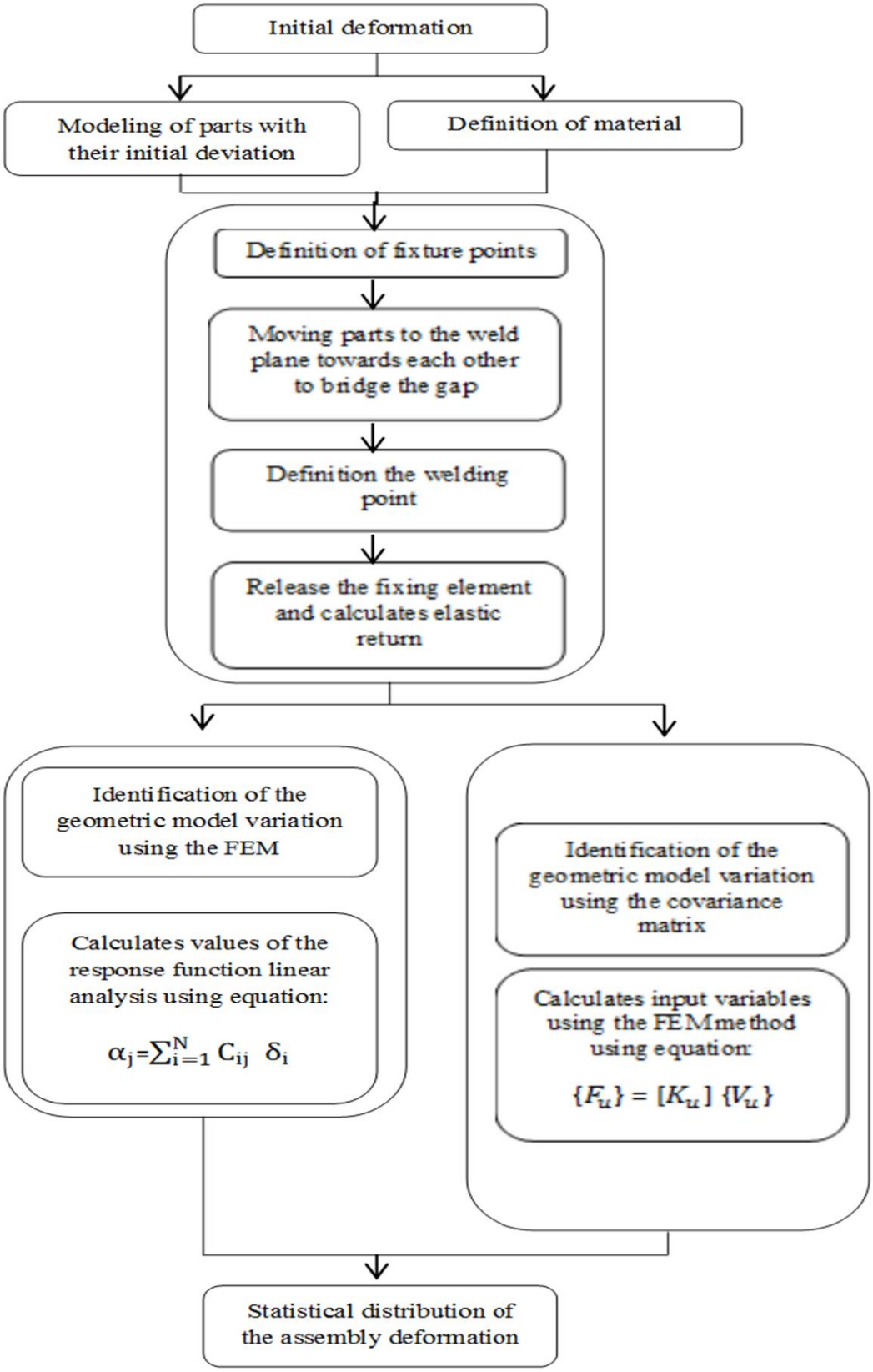

Figure 5. Finite element modeling non-linear analysis and Influence Coefficient Method linear analysis of the flexible assembly process.

The first one is the Influence Coefficient Method for tolerancing of flexible parts and assemblies corresponds to a method of disturbance where the quantities of interest that will be noted αj as the sum of the products of each contributor, denoted δi and of coefficients of influence cij determined by assembly simulations of these parts. The equation shows this approximation in index and matrix notation.

$$\alpha_j = \sum_{i=1}^{N} C_{ij}\ \delta_i \quad (6)$$

The Influence Coefficient Method supposed linear C_{ij} characterize the influence that the contributor numbered i on the quantity of interest numbered j. The matrix [S] is the "sensitivity matrix"; it contains all the influence coefficients of the contributor on the quantity of interest.

The second one is the nonlinear method based also on the FEM. The proposal method is shown in the Figure 5.

7. ANALYSIS MODEL AND LOADING CONDITIONS

Figures 6,7 show the analysis model which consists of two parts of sheet metal with 0,5 mm thick for both of them. The two parts are superposed, and two copper alloy electrodes are simultaneously used to clamp the sheets together. The surfaces are only mechanically contacted.

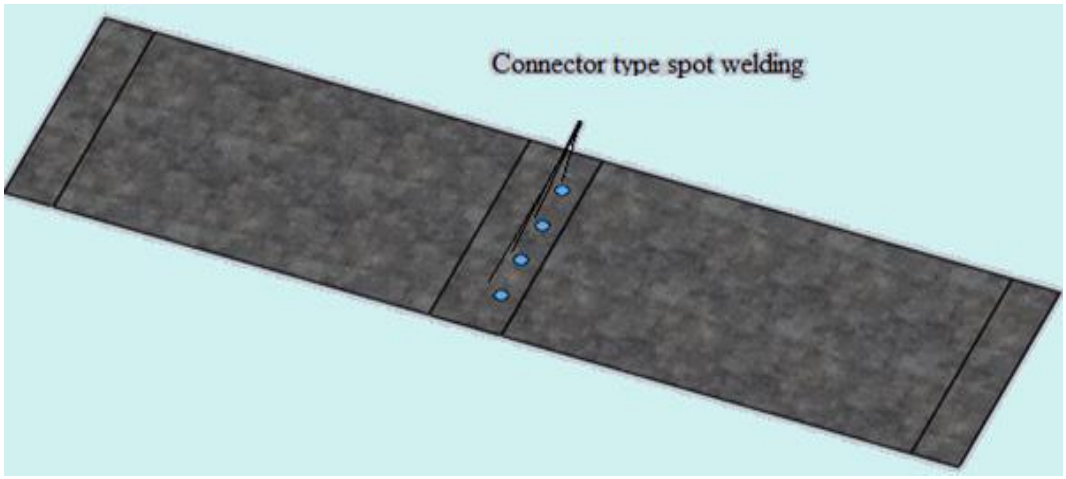

Figure 6. Geometrical model of the plate assembly.

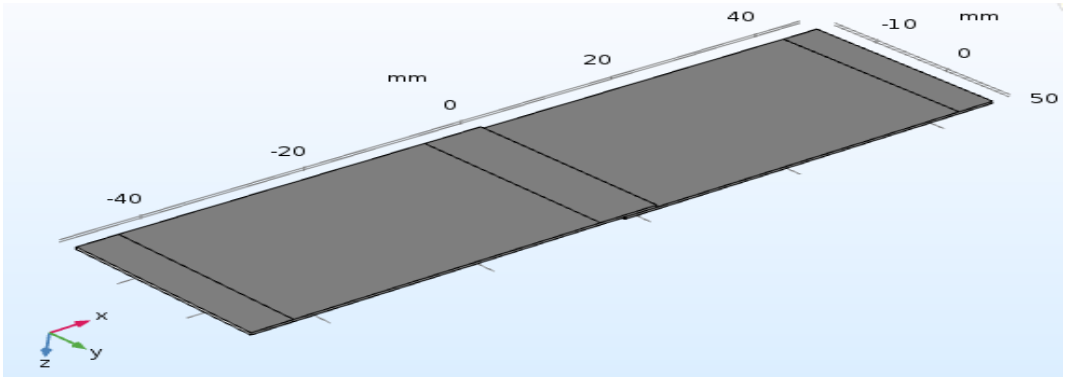

Figure 7. Plate geometry.

7.1 Object of the study

The aim of this study is to analyze the influence of these deviations on final product; one solution is to generate the Skin Model Shape based on a linear to simulate assembly with the consideration of spot-welding effects, the second one is to generate the Skin Model Shape this time based on a nonlinear to simulate assembly with the consideration of spot-welding effects. The global principle of both of the methods is based on finite element analysis. The first one is nonlinear finite element analysis but then we use a linear method Influence Coefficient (MIC) with the linearization of the deviations by the spot-welding function approach. In order to check the geometrical conformity of the both simulation of the assemblies knowing that the connection is a spot welding. We will model faults of 2000 assembly; the contributors have a normal distribution with a mean $\mu = 0$ and a standard deviation $\sigma = 1$.

7. 2. Results

An assembly of two identical flat sheet metal components by spot welding shown in the previous figure is employed to illustrate the proposed method. The parts are modeled and meshed with linear and nonlinear elements using the ABAQUS software. The set consists of 4400 elements. The sources of variation of the piece are considerate and declared with the same software. The discretization of the problem is presented in Figure 8.

In order to verify and test the implemented spot-welding effects algorithm in MIC and FEA, two different simulations for the same geometry and variation are performed:

- Influence Coefficient Method with the consideration of spot-welding effects (linear)
- Finite element analysis with the consideration of spot-welding effects (nonlinear).

The final displacement for all nodes after the springback deflection is recorded and presented for all iteration in Figure 9 and 10. The same set of variables has been used in all simulations.

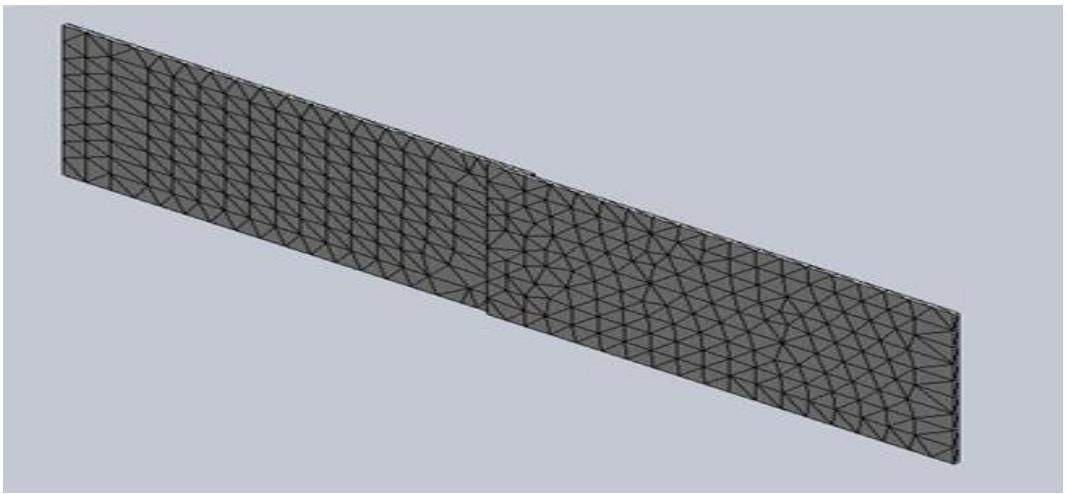

Figure 8. The finite element computation model of two sheet metal parts assembly.

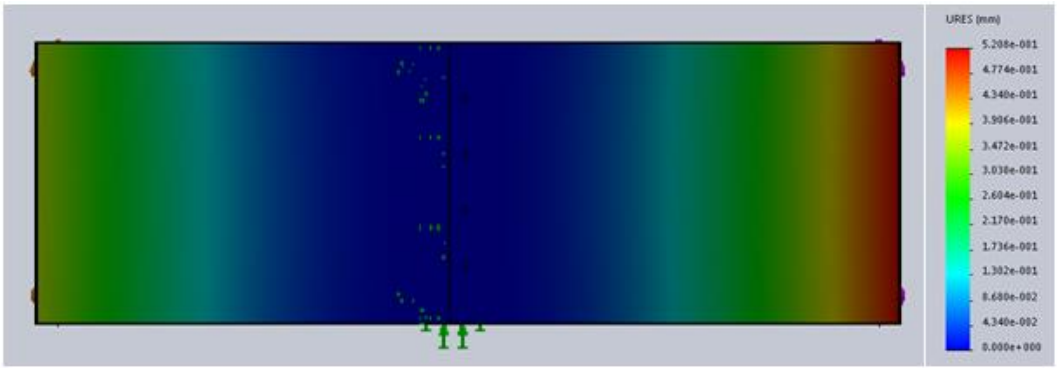

Figure 9. Results of the distribution of the dimensional variations of the assembly by the modelization with spot welding by MIC.

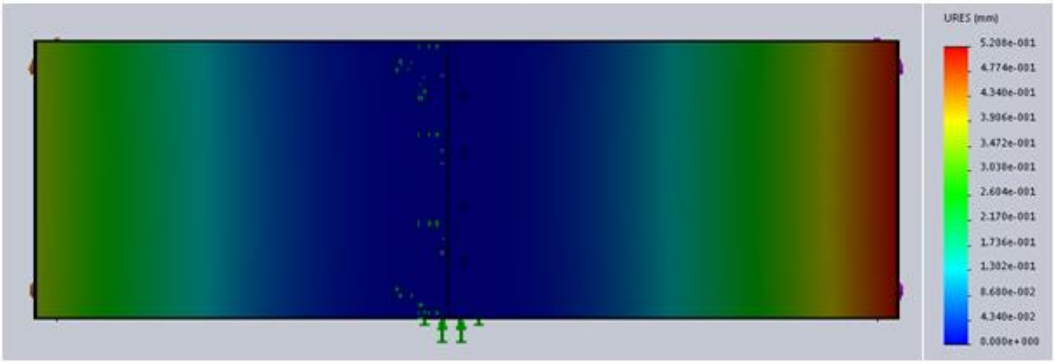

Figure 10. Results of the distribution of the dimensional variations of the assembly by the modelization with spot welding by non-linear method.

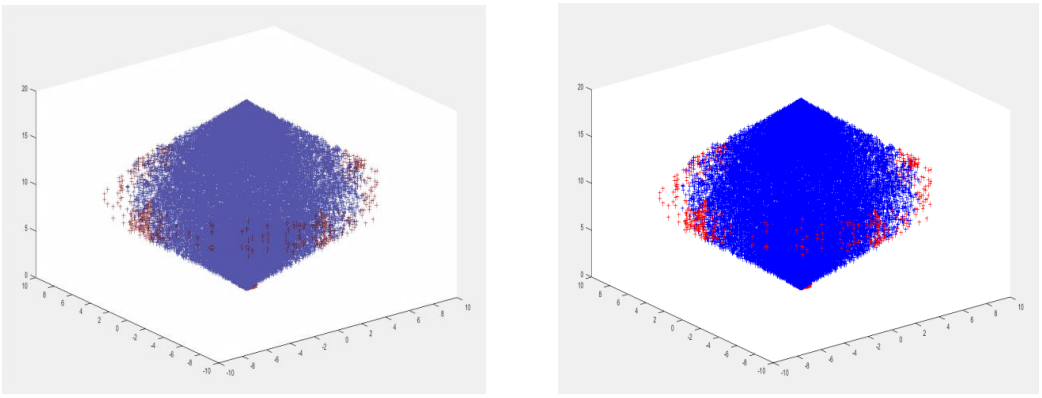

Figure 11. Geometrical conformity of the assemblies with nonlinear analysis with spot welding and, linear analysis with spot welding.

To verify the geometrical conformity of the assemblies knowing that the connection is complete, we will model the defects of 2000 assemblies. The contributors have a normal distribution with mean $\mu = 0$ and standard deviation $\sigma = 1$. The results of the simulation are shown in Figure 11. The observed non-compliance rate is 4.05% for nonlinear analysis with spot welding and 4.042 for linear analysis with spot welding.

The comparison shows that the result of the Influence Coefficient Method (MIC) with the consideration of spot-welding effects (linear) is almost identical to the result of the Finite element analysis with the consideration of spot-welding effects (nonlinear). This means that the MIC method with linear variation can be used for the simulation and analysis of deformable assemblies.

CONCLUSION

We compare two results obtained from the simulations of the parts with two solutions. The first solution is to generate the Skin Model Shape based on a linear to simulate assembly with the consideration of spot-welding effects, the second one is to generate the Skin Model Shape this time based on a nonlinear to simulate assembly with the consideration of spot-welding effects; in order to check the geometrical conformity of the both simulation of the assemblies. According to the last simulations the comparison shows that the result of the linear simulate assembly is almost identical to the result of a nonlinear simulate assembly. This means that the linear simulation of the flexible assembly with the consideration of spot-welding effects can be used for simulation and analysis of flexible assemblies with a high precision and in a very short time with 7 second by contributing to 1236 second for the nonlinear simulation the assembly with the consideration of spot-welding effects.

REFERENCES

[1] S. C., Liu and S. J. Hu, *Journal of Manufacturing Science and Engineering*, **119(3)**, 368 (1997).
[2] S.C. Liu, S.J. Hu and T.C. Woo, *ASME J. Mech. Des.* **118 (1)**, 62 (1996).
[3] A. Stricher, L. Champaney, F.Thiebaut, B. Fricero and N. Chevassus,*12th National Colloque AIP PRIMECA*, no. 1, p. 1 (2011).
[4] A. Stricher, ENS Cachan (2013).
[5] J. A. Camelio, S. J. Hu and D. Ceglarek, *Journal of Mechanical Design*, **125(4),** 673 (2003).
[6] H. Atik, M. Chahbouni, D. Amegouz and S. Boutahari, *International Journal of Engineering &Technology*, **7(1),** 85 (2018).
[7] H. Atik, M. Chahbouni, D. Amegouz and S. Boutahari, *International Journal of Engineering &Technology*, **7(1),** 90 (2018).
[8] X. Yan and A. Ballu, *Int. J. Adv. Manuf. Technol.* **92(1-4),** 789 (2017).
[9] L. Homri, E. Goka, G. Levasseur and J.-Y. Dantan, *Computer Aided Design*, **91**, 46 (2017).
[10] M. Chahbouni, S. Boutahari, D. Amegouz, *International Journal of Engineering &Technology*, **3(3)**, 343 (2014).

Nanomaterials Science & Engineering (NMS&E), Vol.1, No.1, 2019

Department of Mechanical Engineering
University of Aveiro
Aveiro 3810-193
Portugal

https://proa.ua.pt/index.php/nmse/

ISSN: 2184-7002

university of aveiro  tema centre for mechanical technology and automation